



City Research Online

City, University of London Institutional Repository

Citation: Kyriazis, N., Koukouvinis, F. & Gavaises, E. (2018). Modelling cavitation during drop impact on solid surfaces. *Advances in Colloid and Interface Science*, 260, pp. 46-64. doi: 10.1016/j.cis.2018.08.004

This is the preprint version of the paper.

This version of the publication may differ from the final published version.

Permanent repository link: <https://openaccess.city.ac.uk/id/eprint/21973/>

Link to published version: <https://doi.org/10.1016/j.cis.2018.08.004>

Copyright: City Research Online aims to make research outputs of City, University of London available to a wider audience. Copyright and Moral Rights remain with the author(s) and/or copyright holders. URLs from City Research Online may be freely distributed and linked to.

Reuse: Copies of full items can be used for personal research or study, educational, or not-for-profit purposes without prior permission or charge. Provided that the authors, title and full bibliographic details are credited, a hyperlink and/or URL is given for the original metadata page and the content is not changed in any way.

City Research Online:

<http://openaccess.city.ac.uk/>

publications@city.ac.uk

Modelling cavitation during droplet impact on solid surfaces

Nikolaos Kyriazis^{a,*}, Phoivos Koukouvinis^a, Manolis Gavaises^a

^a*School of Mathematics, Computer Science & Engineering, Department of Mechanical Engineering & Aeronautics, City University London, Northampton Square EC1V 0HB, United Kingdom.*

Abstract

The impact of a liquid water droplet on a solid surface at conditions inducing cavitation inside its volume has rarely been addressed in the literature. A review is conducting on relevant studies, focusing mainly on the numerical models suitable for droplet impact at such conditions. The process is also investigated by developing a compressible two-phase flow model that incorporates a phase-change suitable for cavitation formation and collapse. Thermodynamic closure is based on a barotropic Equation of State (EoS) representing the density and speed of sound of the co-existing liquid, gas and vapour phases as well as liquid-vapour mixture. To overcome the known problem of spurious oscillations occurring at the phase boundaries due to the rapid change in the acoustic impedance, a new hybrid numerical flux discretization scheme is proposed, based on approximate Riemann solvers; this is found to offer numerical stability and has allowed for simulations of cavitation formation during droplet impact droplet to be presented for the first time. Following a thorough justification of the validity of the model assumptions adopted for the cases of interest, numerical simulations are firstly compared against the Riemann problem, for which the exact solution has been derived for two materials with the same velocity and pressure fields. Following, the model is validated against the single experimental data set avail-

*Corresponding author

Email addresses: Nikolaos.Kyriazis@city.ac.uk (Nikolaos Kyriazis), Foivos.Koukouvinis.1@city.ac.uk (Phoivos Koukouvinis), M.Gavaises@city.ac.uk (Manolis Gavaises)

able in the literature for a 2-D planar droplet impact case [1]. The results are found in good agreement against these data that depict the evolution of both the shock wave generated upon impact and the rarefaction waves, which are also captured reasonably well. Moreover, the location of cavitation formation inside the droplet and the areas of possible erosion sites that may develop on the solid surface, are also well captured by the model. Following model validation, numerical experiments have examined the effect of impact conditions on the process, utilising both planar and 2-D axisymmetric simulations. It is found that the absence of air between the droplet and the wall at the initial configuration can generate cavitation regimes closer to the wall surface, which significantly increase the pressures induced on the solid wall surface, even for much lower impact velocities. A summary highlighting the open questions still remaining on the subject is given at the end.

Keywords: Cavitation, droplet impact, approximate Riemann solvers, OpenFOAM

1. Introduction

Droplets impacting onto solid or liquid surfaces are of significant importance in many engineering applications, oceanography, food science and even forensics; see selectively [2, 3, 4, 5, 6] among many others. For isothermal conditions, the Weber We, Reynolds Re, Ohnesorge Oh and Froude Fr numbers are frequently utilised to characterise the droplet impact outcome; these are defined as

5 Weber We, Reynolds Re, Ohnesorge Oh and Froude Fr numbers are frequently utilised to characterise the droplet impact outcome; these are defined as

We = $\frac{\rho_l u_{imp}^2 D}{\sigma}$, Re = $\frac{\rho_l u_{imp} D}{\mu_l}$, $Oh = \frac{\sqrt{We}}{Re}$ and Fr = $\frac{u_{imp}}{\sqrt{gD}}$ respectively. In these relations, u_{imp} is the impact velocity normal to the wall surface, D is the droplet diameter, μ_l and ρ_l are the dynamic viscosity and density of the liquid

10 droplet respectively, σ is the surface tension and g is the gravitational acceleration. A number of post-impact outcomes are known for the normal/inclined impact of spherical droplets onto flat and smooth surfaces [7, 8]. In the vast majority among the cases of practical interest, the flow conditions and the evolution of the droplet shape upon impact can be described assuming that the

15 liquid and the surrounding media behave as incompressible media. Still, out of
the very broad literature on the subject, or interest to the present paper are
the cases of impact at velocities of the order of 200 m/s ($M \approx 0.6$ for air at
room temperature and atmospheric pressure) which are high enough for com-
pressibility effects to become important. Moreover, at such conditions pressure
20 waves developing within the liquid during impact may induce cavitation for-
mation within the droplet volume. Cavitation as a phenomenon involves the
formation of vaporous/gaseous cavities in the bulk of liquid, due to localized
static pressure drop. This can happen due to strong accelerations, high veloci-
ties or pressure waves. In the first case, cavitation is termed as 'hydrodynamic'
25 and may occur in any device operating with liquids, e.g. propellers, turbines,
pumps, valves etc. In the second case, cavitation is termed as 'acoustic', since it
is induced by the presence or interaction of acoustic waves. Phase-change dur-
ing cavitation is inertial driven [3] as opposed to temperature difference driven.
Moreover, for the high impact velocity conditions leading to cavitation forma-
30 tion, the impact outcome is expected to be in the splashing regime, where a
corona is initially formed and gradually disintegrates into a number of droplet
fragments. Such impact velocities can be realised, for example, in steam turbines
and aircraft components. The steam in the turbine engine operating at low pres-
sure conditions is prone to condensation and thus, water droplets are formed.
35 These droplets travel with the flow and can impact the turbine blades with high
speeds [4, 9]. The problem is further complicated by the subsequent cavitation
formation and collapse induced by the pressure waves developing within the
droplet's volume. At such conditions, surface erosion and damage may occur,
not only because of the impact pressure, but also due to the pressure increase
40 occurring during the collapse of the cavitation bubbles. The early experimental
work of Field et al. [10] documented that the edge pressures depend on the
impact velocity and the angle between the liquid and the solid surfaces (see also
[11]). More recently, Field et al. [1] presented high-speed images of impacted
liquids using several different techniques. By adding gelatine in the water, they
45 produced 2-D planar 'droplets' between two transparent plates while impact

was achieved by a projected third plate. The shock waves produced and the resulting vapour formation due to cavitation within the bulk of liquid has been observed qualitatively. So far, no other studies are known in this field. The present paper aims to contribute to this area by conducting initially a literature
50 review on the subject, followed by numerical simulations from a purpose-built computational model. The literature reviews starts with a summary of relevant numerical works for droplet impact of incompressible liquids, while touching on phase-change phenomena observed at elevated wall temperatures and the role of wettability. Then a short review on phase-change models and numerical
55 methodologies for cavitation, relevant to the current study is included, followed by a review of the studies that have addressed the role of compressibility during droplet impact. As there is no computational work reported in the literature for droplet impact in the presence of cavitation formation and subsequent collapse, the paper presents results from a newly developed computational fluid
60 dynamics flow solver suitable for such conditions. Following validation against the experiments of Field et al. [1], parametric studies aim to provide further insight on the problem physics.

2. Literature Review

2.1. Summary of methodologies applied to droplet impact assuming incompressible liquids 65

Both experiments and complex numerical simulations based on the solution of the Navier-Stokes equations have been utilised to characterise the impact process of liquid droplet onto solid or liquid surfaces. Within the context of incompressibility and at conditions that surface tension (i.e. sufficiently small
70 We numbers) dominates the temporal development of the phenomenon, Lagrangian (interface tracking) and Eulerian (interface capturing) approaches, or even a combination of the two have been utilised to simulate the process. For example, Harlow and Shannon [12] were the first to utilise the Lagrangian approach using a marker-and-cell (MAC) finite difference algorithm ignoring

75 surface tension and viscosity while, the volume of fluid (VOF) model was introduced by Hirt and Nichols [13]; later Youngs [14] proposed a 3-D volume tracking algorithm (see also [15]). Aniszewski et al. [16] made a comparative study among different VOF methodologies. Numerous follow-up studies have addressed the problem under various impact conditions [17, 18, 19], different fluids [20], elevated wall temperatures [21], impact on non-flat [22, 23] or complex [24] surfaces and impact of stream of droplets [25, 26]. Apart from the VOF method, the Piece-wise linear Interface Calculation (PLIC) approach [27, 28], the Weighted Linear Interface Calculation (WLIC) method, which was introduced by Yokoi [29] and independently by Marek et al. [30] and the Tangent of Hyperbola for Interface Capturing (THINC) interface reconstruction scheme, 85 which was described by Xiao et al. [31]; the more recent works of [32, 33] are an extension of THINC scheme. Fukai et al. [7] developed a finite element model (FEM) for the incompressible flow equations but the hyperbolic character of the equations was obtained by the artificial compressibility method. Although 90 the VOF method was originally developed and has been mainly used for incompressible flows, it has been also extended to compressible fluids, see for example [32, 34, 35, 36, 37, 38]. Nowadays, VOF methods with arbitrary unstructured meshes have become popular and have been implemented in the open source CFD toolbox OpenFOAM [39, 40]. Along these lines, Gerris, an open source incompressible VOF solver with adaptive mesh refinement capabilities, originally 95 developed by Popinet [41], has been used for two-phase flows where surface tension is prevalent but without modelling phase-change phenomena (see also [42]). Overall, such methods are in principle applicable to cases with cavitation developing during the droplet impact; however, as it is demonstrated later, accurate 100 modelling of the liquid-gas interface becomes important at time scales much longer than the cavitation formation and collapse, and thus these methods are less important or can be even not accounted for such problems.

2.2. Phase-change phenomena during droplet impact induced at elevated temperature conditions

105 Droplet impact occurring at temperature differences between the impacting liquid and the solid target are important for many heating/cooling applications as well as physical systems. Numerous studies are available for cases where phase-change phenomena take place during droplet impact. Almost exclusively, such phenomena are thermally driven, as opposed to pressure-driven (cavitation) 110 phase-change. Depending on the temperature, pressure, liquid properties [43] and surface wall conditions [44], surface wettability (contact angles) [45, 46], various post-impact regimes have been identified, such as contact evaporation (stick), nucleate boiling, film boiling, rebound (Leidenfrost) with or without breakup and splashing [44, 47, 48, 49]. The latter is observed for sufficiently 115 high We numbers; surface temperature and the induced heat transfer are known to dominate the process. Similarly, liquid vaporisation can occur when droplets are moving within a surrounding hot air environment. Such conditions prevail in combustion engines [3] and fluidised beds [50]. On the modelling aspect of such processes, most efforts simulate phase-change through vaporisation of the 120 liquid-gas interface. The first works on droplet evaporation employed a body-fitted grid at the liquid-gas interface, rendering the methodology applicable only for 2-D axisymmetric problems. This approach has been used for single [51] and multicomponent [52] spherical droplets, as well as at high pressure conditions [53]. Pasandideh-Fard et al. [21] were the first who developed a 125 VOF method for modelling heat transfer during droplet impingement. Later on, Strotos et al. [54] employed a VOF method in connection with a local evaporation model based on the kinetic theory aiming to study the phase-change on the droplet interface and the heat transfer between the surrounding air, the droplet and the wall (see also [55]). Harvie et al. [56] simulated droplet 130 impacts on hot surfaces; they employed an implicit pressure-based algorithm for the incompressible Navier-Stokes equations. The interface of the droplet is captured by the VOF model which is coupled with an 1-D algorithm for the flow in the viscous vapour layer and the heat transfer within the solid, liquid and

vapour phases (vapour layer model). Some other researchers employed semi-
135 analytical and experimental approaches for evaporation and heat transfer in
droplets [57, 58, 59, 60, 61]. VOF methodologies for tracking the free surface
of droplets impacting a solid surface have been also developed by Pasandideh-
Fard et al. [62, 63], Rieber and Frohn [64], Bussmann et al. [22] and more
recently the author's group and co-workers, see Malgarinos et al. [65]. In order
140 to have a more accurate reconstruction of the interface, Guo et al. [8] invoked
the moment of fluid (MOF) method to investigate droplet impingement and
splashing on dry and wet surfaces. In the MOF method, which is an extension
of the VOF model, the centroid of each material is integrated along with the
volume fraction for each material. A number of studies also deal with nucleate
145 boiling within the impacting droplet, which greatly modifies the impact outcome
(see for example [60]). Numerical works on nucleate boiling employ VOF and
Level-Set methods for treating the different phases [66]. Still, the time scale
in nucleate boiling phenomena is significantly larger, compared to cavitation
phenomena [67]. This can be demonstrated through the Jakob number, which
150 is of the order $Ja \sim 760$ and therefore, the flow is inertia driven [68]. Thus, the
relevant models are not applicable to the cases considered here.

2.3. The role of wettability

Wettability is known to be one of the most influential parameters during
droplet impacts. Depending on surface wettability (or the contact angle θ_c), sur-
155 faces are classified into hydrophobic ($\theta_c \gg 90^\circ$) and hydrophilic ($\theta_c \ll 90^\circ$).
This surface characteristic is of significant importance and has been studied
extensively, both experimentally and numerically, due to its industrial appli-
cations, for instance in heat transfer or to avoid adhesion of dirt. Moita and
Moreira [69] investigated experimentally the effect of wettability and surface
160 topography during water and fuel droplet impacts. They used different ma-
terials for the impact surface, such as aluminum, steel, copper and glass (see
also [24, 70]). From a numerical point of view, in order to model a realistic
behaviour of the surface, contact angle models have been developed. The most

common approach is to implement contact angle boundary conditions at the
165 computational cells adjacent to the wall [65]. Fukai et al. [17] were the first
who adjusted the contact angle during droplet impact by implementing appropriate
boundary conditions. Another approach which has been followed in several works
[62, 71, 19, 72], was originally proposed by Brackbill et al. [73], is the CSF
model. In the latter, the surface tension force is modified accordingly
170 by changing the normal vector at the free surface in order to define the contact
angle. While static contact angle approximations are sufficient for low velocity
impacting droplets, the more complete dynamic contact angle models [23] have
been proposed for higher We droplet impacts, but for cases where surface tension
is taken into consideration. The most prevalent dynamic contact angle
175 approaches are the quasi-dynamic contact angle model [21], Kistler’s law [74],
Shikhmurzaev’s model [75] and the wetting force model, based on the work of
Antonini et al. [76]. The wettability of the impacting droplet is also strongly
related to the surface topography. Although there are several experimental studies
investigating the effect of surface roughness on droplet impacts [77, 69, 70], this
180 is not feasible when employing the conventional numerical methods. In order
to model surface roughness, CFD analysis to a sub-micron level must be performed,
which renders such simulations unfeasible. The only available numerical studies
utilise molecular dynamics simulations (see for example [78]) aiming to model
surface topography.

185 To the best of the author’s knowledge, there is no study that addresses the
possible influence of wettability during cavitation collapse near walls. In the
absence of relevant studies, this area remains open for further investigations
and it is not addressed here.

2.4. Models for cavitation and interaction with surfaces

190 As the physics and relevant models for cavitation are the primary focus of the
present work, an extended summary of models is provided. The review considers
models applicable both to microscales (single bubble collapses) or cavitation
clouds comprising a large population of bubbles and thus more suitable for

problems of engineering interest. The thermodynamic closure of such models is
195 also briefly addressed; finally models suitable for cavitation erosion are briefly
mentioned; these are relevant to the interaction of cavitation with surfaces but
they go beyond the focus of the present work.

2.4.1. Models suitable for single-bubbles (microscales)

From a historical perspective, interaction of cavitation bubble collapse with
200 a nearby solid surface has been studied since 1970 [79]. Along similar lines are
the investigations of [80, 81] on bubble deformation and collapse near a wall, em-
ploying the Boundary Element Method (BEM). This method is still being used
for high fidelity bubble simulations [82] and interactions with deformable bod-
ies [83, 84]. Despite its relative simplicity and accuracy, BEM is susceptible to
205 instabilities and it is difficult to handle topological changes of the bubble inter-
face [85], which require regularization and smoothing. Moreover, the potential
solver, at the core of BEM, lacks small scale dissipative mechanisms leading to
singularities [86]. Extensions of BEM involve Euler/Navier-Stokes flow solvers,
which may include compressibility effects as well and sharp interface/ interface
210 capturing/tracking techniques [87]. More recent work employs multiphase flow
techniques for handling of the gas/liquid interface [88, 89] using a Homoge-
neous Equilibrium Model. Apart from single fluid approaches, various interface
tracking methodologies have been employed for the prediction of pressure due
to bubble collapse. A notable example of high-end simulations of bubble cloud
215 collapse is [90]; the authors performed simulation of a resolved bubble cloud,
consisting of 15,000 bubbles in the vicinity of a wall, using a supercomputer.
Representative studies using the Volume Of Fluid (VOF) approach to predict
bubble collapses and jetting phenomena include [91, 92, 93]. Instead of VOF,
other authors [94, 95] used the Level Set (LS) technique for analyzing the effect
220 of different bubbles at different distances from nearby walls. Both techniques
have their advantages and disadvantages; VOF ensures conservation, whereas LS
offers high accuracy calculation of the interface curvature and surface tension.
An alternative to interface tracking methodologies is the front tracking method

[86], such as the one used in [96] for the simulation of gas bubbles collapsing in
225 finite/infinite liquid domains. This method differs from VOF or LS, in the sense
that the interface is explicitly tracked by a set of Lagrangian marker points that
define the interface topology, enabling high fidelity simulations and predictions
to be made, without smearing of the interface. Assessing current methodologies,
the treatment of the vapour/gas and liquid mixture, both Homogeneous Equilib-
230 rium [89] or non-equilibrium interface tracking immiscible fluid methodologies
are applicable. While both methodologies have been successfully employed for
studying the pressure field generated on the wall due to the collapse of nearby
bubbles for various configurations, the methodology of interface capturing is
definitely less restricting, allowing one to simulate gaseous/vaporous mixtures
235 within the bubble, while also prescribing finite rate of mass transfer and giv-
ing the opportunity of imposing surface tension, which is important in the case
of bubble nucleation. The front tracking method has the advantage of being
capable of incorporating the capabilities of the interface tracking and the two
fluid approach, without interface diffusion; however, it is somewhat problematic
240 in complicated interface topologies [97]. With regards to simultaneous simula-
tions of pressures resulting from the collapse of cavitating bubbles and material
response to induced load, very few studies have been published [98, 99, 100].

2.4.2. Cavitation models suitable for engineering scales

Cavitation models applied to length/time scales of practical or engineering
245 interest, can be classified into three categories. The first approach invokes the
thermodynamic equilibrium assumption, leading to an effective mixture equa-
tion of state that returns the vapour volume fraction directly from the cell-
averaged fluid state [88]. As this mixture model constitutes a natural sub-grid
scale model for the thermodynamic fluid state, recovering the limit of individ-
250 ual bubbles for sufficient resolution, it seamlessly can be employed within a
physically motivated implicit LES approach [101]. Whereas all practical appli-
cations in engineering relevant cases at high ambient pressures indicate that the
equilibrium model give the correct prediction in terms of cavitation and wave dy-

namics, detailed investigations of incipient cavitation or wall-bubble interactions
255 may depend on other processes, for example, gas content, wall crevices and local heating effects. For such phenomena at single bubbles, interfacial effects are potentially important and can be treated by sharp-interface methods [102, 88]. The second approach is based on the introduction of a rate equation for the generation of vapour that employs explicit source/sink terms. Both Eulerian-
260 Eulerian and Eulerian-Lagrangian formulations can be used to track the vapour production and its interaction with the liquid. For example, Eulerian-Eulerian models use a bubble-cloud model applied to Reynolds-averaged turbulence modelling [103, 104] and LES. In the model of [105] instead of treating cavitation as a single mixture, the two-fluid method was employed; two sets of conservation
265 equations are solved, one for the liquid and one for the vapour phase. With this approach the two phases can have different velocities. Another variant of the bubble model is the approach of [106, 107] in which the classical interface capturing Volume of Fluid (VOF) method was utilised for simulating the scalar volume fraction of a bubble cloud. Similar models are currently available in
270 commercial CFD models [108, 109, 110]. Typically, these models utilize the asymptotic form of the Rayleigh-Plesset equation of bubble dynamics. They all require information on the bubble number density and population present in the liquid prior to the onset of cavitation, while, depending on their complexity and sophistication, they may include or ignore mass transfer between the liquid
275 and the vapour phases and may consider or not gas content in the liquid. It is clear that at their current state such models require case-by-case tuning of the involved parameters in order to predict realistic cavitation images.

The Eulerian-Lagrangian formulation also aims to provide a coupling between the interaction between the liquid (Eulerian) and vapour (Lagrangian)
280 states. One of the most important models in this category is the Lagrangian cavitation model of [111, 112] that use the Rayleigh-Plesset equation of bubble dynamics for estimating the cavitation volume fraction. More recent advances (selectively [113, 114, 115]) have proposed models that account collective compressibility and shock wave interaction effects in polydispersed cavitating flows.

285 Some models do exist for predicting the collapse process of individual vapour/air
bubbles or bubble clouds within the bulk of the liquid or even near a wall sur-
face (selectively [116, 117, 118, 119]) but most of them have not been applied
to flows of industrial interest while effects such as chemical composition change,
heat transfer and liquid heating are ignored. It is also worth mentioning that
290 effects of dissolved gas, multi-component fluids (such as fuels) and pre-existing
nucleation sites in the fluid have not been investigated so far.

The third approach for describing cavitation effects is by employing Proba-
bility Density Functions (PDF) and related transport models. In [120] a PDF
transport model is used for the vapour fraction, based on the Boltzmann trans-
295 port equation, in order to model the highly dynamic and stochastic interaction
of the turbulent flow field with the cavitation structures. An additional novelty
of [120] is the fact that the solution of the PDF is done entirely in an Eule-
rian framework, avoiding the expensive cost and the inaccuracies induced by
coupling an Eulerian and Lagrangian solver. The authors have shown that by
300 coupling the PDF method with a compressible LES framework, they obtained
good results for a variety of Venturi-like tubes and shapes. The applicability
of such models to engineering-scale problems has not been tested yet. Finally,
apart from the aforementioned models, which are based on the finite volume
framework, there have been efforts for describing cavitation using alternative
305 frameworks. Examples of such works may include (a) simulation of cavities
due to the entry of high speed objects, using the mesh-less Smoothed Particle
Hydrodynamics (SPH) [121] and the Finite Element method (FEM) [122], (b)
simulation of cavities at the wake of submerged bodies in liquid [123], using
Distributed Particle Methods and focusing on the SPH method in particular,
310 (c) simulations of forward step geometries, resembling the orifice of injectors,
using Lattice Boltzmann methodologies [124]. These examples are, of course,
non-exhaustive. There are many different approaches, most of them at an in-
fancy stage, for attacking the phenomenon of cavitation, each having specific
advantages and disadvantages on specific flow types. On the other hand, the
315 Finite Volume framework is mature enough and offers better handling of the

underlying flow phenomena with less uncertainties over the physics for general flow types.

2.4.3. *Thermodynamic closure*

A common issue that is found in bubble dynamics simulations in the recent literature is the EoS of the materials involved and, more generally, material properties and their variation in respect to pressure and temperature. It is well known that gas/vapour bubbles may be at sub-atmospheric conditions when at maximum size, but during the last stages of the collapse pressures may reach the order of GPa and temperatures of several thousand degrees K. In the literature, however, it is commonly assumed that liquids behave according to the stiffened gas EoS and the gas/vapour as an ideal gas [90, 125, 126] despite the strong evidence that the stiffened gas EoS may not be adequate, since it cannot replicate at the same time both the correct density and speed of sound of the liquid [127]. For this reason, many researchers have recently turned towards more accurate relationships for describing the materials involved [89] and [128] developed by the authors. Such accurate EoS have been formulated by NASA [129, 130] or in other investigations [131].

2.4.4. *Cavitation erosion*

With regards to cavitation erosion, two concepts can be followed. The first concept is to calculate the whole cavity development from macro to micro scales. These computations attempt to model the shock waves that are produced upon the collapse of a cavity bubble cluster, where the kinetic energy flux from the liquid flow is largely converted into the acoustic power associated with the shock waves that are emitted upon collapse. It is hypothesized that it is these shock waves that produce the most important mechanism causing erosion of the nearby located material [132]. Early attempts to quantify the erosive action from imploding cavity clouds are given by [133, 88, 134, 135]. These models are based on the collapse of bubbles that are generated by breaking up sheet cavitation. Empirical relations can be used for the initial number

size distributions of these bubbly clouds while fully compressible formulation of the liquid/vapour phases have been used, in order to capture the shock waves. Clearly, such models have a limitation on the resolution that can be employed and the initial conditions employed. The other concept attempts to separate the flow problem into a large scale problem that can be addressed by e.g. a multi-phase RANS/LES solvers and a micro-scale problem that can be addressed by either a numerical model or by a semi-empirical erosion model or damage functions [136, 137, 138, 139, 140, 141, 142, 143]. The developed correlations are based on generic concepts of the acoustic pressure emitted upon bubble collapse, the formation of micro-jets or even on the absolute pressure itself, the number of collapsing bubbles, the energy cascade from large structures to smaller ones or the potential energy contained in a shed cavity exceeds a certain damage threshold. Nevertheless, these correlations, despite they have given promising results in some cases, they do not predict damage itself but aim to indicate locations more vulnerable to erosion; moreover, no correlation can claim a universal validity. To this end, the present paper is not making a new contribution to the known literature. It can be however mentioned that the develop solver is generic and thus, it can be in principle combined with any surface erosion model available.

2.5. Droplet impact and cavitation formation

The aforementioned studies regarding cavitation have never been applied so far to cases of droplet impact. There are some studies addressing compressibility effects but have been considered only a small part of the relevant literature. The analytic solutions of Heymann [144] and Lesser [145] were the first who considered compressibility. Heymann [144] performed a quasi-steady state 2-D analysis of the dynamics of impact between a compressible liquid droplet and a rigid surface. However, this analysis is only valid for the initial stages of the impact, during which the shock is attached to the solid surface, so the jetting in the contact edge could not be predicted. Later on, Lesser [145] expanded this work and took into account the elasticity of the surface while he

375 also gave an analytic solution of the 3-D droplet impact problem. Numerical
simulations have been also employed. For example, a front tracking solution
procedure was invoked by Haller et al. [146] for high-speed impact of small
size droplets. A rectangular finite difference Eulerian grid and a moving lower
dimension Lagrangian one to track the location of the wave fronts have been
380 utilized (see also [147]). In another compressible approach, Sanada et al. [148]
used the multicomponent Euler equations to model high-speed droplet impact.
They developed a third-order WENO scheme with an HLLC Riemann solver
and the time advancement was achieved by a third-order TVD Runge-Kutta.
More recently, Niu and Wang [149] developed a compressible two-fluid model
385 for the Euler equations and they proposed an approximated linearized Riemann
solver for the liquid-gas interface. Surface tension was neglected due to high We
number, as well as in the above high-speed droplet impacts. Furthermore, they
showed that higher impact speed results in higher impact pressure and possible
damage in the solid surface. Algorithms able to handle liquid-gas interface have
390 been also developed by Lacaze et al. [150], Örley et al. [151] and Gnanaskandan
and Mahesh [152] but droplet impacts have not been simulated so far. More
recently, Shukla et al. [34] solved the multi-component compressible flow equa-
tions with an interface compression technique aiming to capture the thickness
of the interface within a few cells.

395 *2.6. The present contribution*

Despite the observations of Field et al. [1], to author's best knowledge,
there is no other experiment and no numerical study published in which the
formation and development and cavitation within the bulk of the impacting
droplet is considered; the only relevant numerical study is the work of Niu
400 et al. [149], where cavitation zones have been identified but without actually
simulating the phase-change process. The aforementioned experimental data of
Field et al. [1] have not been so far simulated by any of the studies available in
the open literature.

This problem is addressed here for the first time using a newly developed

405 numerical algorithm implemented in OpenFOAM. For modelling cavitation the
thermodynamic closure is achieved by a barotropic approach for the three phases
[151]. In order to keep the conservative form of the solved equations, the gas
phase is modelled by a VOF-like method. Moreover, a hybrid numerical flux,
which is free of numerical dispersion in the phase boundaries and suitable for
410 a wide range of Mach number flows, is also proposed. The numerical model is
utilised to demonstrate and quantify the effect of pressure-driven phase change
taking within the droplet’s volume during the initial stages of impact. The pres-
sures induced on the solid wall during the collapse of cavitation are computed as
function of the impact conditions and are compared to those resulting from the
415 impact itself. Moreover, the influence they have of the temporal development
of the splashing liquid during the initial stages of impact are explained.

The remaining paper is organized as follows. In the following section, the
numerical method is described, including the EoS for the three phases and
the time/space discretization employed. Then the results are presented and dis-
420 cussed; verification and validation of the numerical method is performed against
the the exact Riemann problem and the 2-D drop impact experiment [1], re-
spectively. Then a parametric study utilising 2-D axisymmetric droplet impacts
is performed for different impact velocities; the most important conclusions are
summarised at the end. Finally, in Appendix A, the methodology for deriving
425 the exact solution to the Riemann problem for the multi-material Euler equa-
tions is discussed; this methodology was used to obtain the exact solution for
the benchmark Riemann problem. In Appendix B, the temperature difference
in an isentropic compression process is calculated, justifying that way the choice
of the barotropic EoS.

430 **3. Numerical Method**

In this section, the developed numerical methodology (2phaseFoam), able
to predict liquid, vapour and gaseous phases co-existence under equilibrium
conditions has been developed in OpenFOAM [153]; this has been based on the

single-phase solver rhoCentralFoam. Initially, the main assumptions adopted
435 for the application of the model to droplet impact cases inducing cavitation are
justified, followed by the mathematical description of the model itself.

3.1. Model assumptions

For the cases of droplet impact investigated here, the flow can be considered
inertia driven since the Reynolds number Re is 10^6 ; typically this is calculated
440 for impact velocity 110 m/s , $D = 10\text{ mm}$, $\rho_l = 998.207\text{ kg/m}^3$ and thus, the vis-
cous effects can be neglected. Moreover, interest is focused primarily during the
initial stages of impact when cavitation formation and its subsequent collapse
take place; these occur during the early stages of splashing which is also inertia
driven, so the solution of the Euler equations instead of the full Navier-Stokes
445 are rendered suitable for capturing the relevant physics. Furthermore, the mini-
mum Weber number We in the present droplet impact simulations is calculated
to be around 10^5 and thus, surface tension is negligible; the minimum Froude
number Fr is 88 and therefore the gravitational forces are insignificant compared
to the inertia ones. Due to the high impact velocities which result in high We
450 and therefore neglecting the surface tension, contact angle boundary conditions
are not explicitly defined. Zero gradient boundary condition in the transport
equation for the gas mass fraction is used at the wall instead (equivalent to a
contact angle of 90°). Surface wettability plays an important role only when a
low velocity field is noticed in the lamella and therefore adhesion forces become
455 significant [24]. However, in the present study the lamella velocity is approxi-
mately 10 times higher than the $u_{imp} = 110\text{ m/s}$ and therefore such effects are
ignored.

In the HEM approach which is followed in the present work, infinite nucle-
ation points and infinite mass transfer are assumed, so thermodynamic equilib-
460 rium is achieved instantaneously. This methodology has been demonstrated to
accurately predict the Rayleigh collapse of vaporous structures (see [151, 154,
155]). Given the original configuration and the final simulation time, which cor-
responds to the early stages of droplet splashing, sharp interface algorithms have

not been used in the present study. The droplet is initially placed next to the
465 wall impinging with velocity u_{imp} into stagnant air and as a consequence, there
is no droplet motion in the air before the impact. The latter would necessitate
sharp interface schemes in order to avoid having a diffusive interface while the
droplet is travelling in the air. In addition, at later stages of splashing, which
are not simulated in the present study, sharp interface algorithms are necessary
470 in order to provide a smear-free interface. Finally, temperature effects are not
taken into account in the present study, since they are negligible. The interested
reader is addressed to Appendix B, where this assumption is justified.

3.2. Governing equations

The three dimensional compressible Euler equations in conservative form are
475 considered:

$$\frac{\partial \mathbf{U}}{\partial t} + \frac{\partial \mathbf{F}_k(\mathbf{U})}{\partial x_k} = 0, \quad \text{in } \Omega, \quad (1)$$

where $k = 1, 2, 3$ denotes the x, y, z directions. The following initial and bound-
ary conditions are used for the PDE system:

$$\mathbf{U}(\mathbf{x}, \mathbf{0}) = \mathbf{U}_0(\mathbf{x}), \quad \text{in } \Omega, \quad (2)$$

$$\mathbf{U} = \mathbf{U}_D, \quad \text{on } \partial\Omega_D, \quad (3)$$

$$\frac{\partial \mathbf{U}}{\partial \mathbf{n}} = \mathbf{U}_N, \quad \text{on } \partial\Omega_N, \quad (4)$$

where

$$\mathbf{U} = \left[\rho \quad \rho Y_g \quad \rho u_1 \quad \rho u_2 \quad \rho u_3 \right]^T$$

480 is the conservative solution vector, ρ is the mixture density, ρY_g is the gas mass
fraction and $\rho \mathbf{u}$ is the mixture momentum. Here the absence of the energy
equation is due to the barotropic approach (see section 3.3), whereas a transport
equation for modelling the non-condensable gas phase is used. The flux tensor

$\bar{\mathbf{F}}$ is the convective term and can be analysed into x , y and z components:

485 $\bar{\mathbf{F}} = [\mathbf{F}_1 \quad \mathbf{F}_2 \quad \mathbf{F}_3]$, where:

$$\mathbf{F}_1 = \begin{bmatrix} \rho u_1 \\ \rho Y_g u_1 \\ \rho u_1^2 + p \\ \rho u_1 u_2 \\ \rho u_1 u_3 \end{bmatrix}, \quad \mathbf{F}_2 = \begin{bmatrix} \rho u_2 \\ \rho Y_g u_2 \\ \rho u_2 u_1 \\ \rho u_2^2 + p \\ \rho u_2 u_3 \end{bmatrix}, \quad \mathbf{F}_3 = \begin{bmatrix} \rho u_3 \\ \rho Y_g u_3 \\ \rho u_3 u_1 \\ \rho u_3 u_2 \\ \rho u_3^2 + p \end{bmatrix} \quad (5)$$

3.3. Thermodynamic Model

A homogeneous-mixture approach is used for describing the liquid, liquid-vapour regime (referred as mixture from now on) and gas phases, which means that the three phases are in mechanical and thermal equilibrium. The mixture density ρ is:

$$\rho = \beta_{lm} [(1 - \alpha_v)\rho_l + \alpha_v\rho_v] + \beta_g\rho_g, \quad (6)$$

In the above relation, the subscripts l, m, g represent the liquid, mixture and gas regimes respectively, whereas lm refers to the liquid-vapour mixture which is governed by a single EoS and it is treated as a single fluid. The density of the component $i = l, m, g$ can be found from:

490

$$\rho_i = \frac{m_i}{V_i} = \frac{Y_i m}{\beta_i V} = \frac{Y_i}{\beta_i} \rho, \quad (7)$$

where β is the volume fraction of the i component:

$$\beta_i = \frac{V_i}{V}, \quad \sum_i \beta_i = 1, \quad (8)$$

Y_i is the mass fraction of the i component:

$$Y_i = \frac{m_i}{m}, \quad \sum_i Y_i = 1, \quad (9)$$

and the local volume fraction can be calculated from the formula:

$$\alpha_v = \begin{cases} 0, & \rho \geq \rho_{l,sat} \\ \beta_{lm} \frac{\rho_{l,sat} - \rho_{lm}}{\rho_{l,sat} - \rho_{v,sat}}, & \rho < \rho_{l,sat} \end{cases} \quad (10)$$

The single fluid model for the liquid and mixture is extended by a transport equation for the non-condensable gas. A linear barotropic model has been utilized for the pure liquid and mixture (lm). The density ρ_{lm} of the latter is:

$$\rho_{lm} = \rho_{l,sat} + \frac{1}{c^2}(p - p_{sat}), \quad c = \begin{cases} c_l, & p \geq p_{sat} \\ c_m, & p < p_{sat} \end{cases} \quad (11)$$

where $\rho_{l,sat}$ is the density of the liquid at saturation condition and c is the speed of sound of the liquid or the mixture, depending on the saturation pressure p_{sat} . The gas phase, has been modelled by an isothermal ideal gas EoS and thus, the gas density is given by:

$$\rho_g = \frac{p}{R_g T_{ref}}, \quad (12)$$

where the reference temperature is $T_{ref} = 293.15 K$ and the specific gas constant is $R_g = 287.06 J/(kg K)$. The barotropic approach is followed since the temperature difference in the following simulations is negligible (the interested reader is referred to Appendix B, where the temperature difference in an isentropic compression process is calculated).

Differentiating isentropically Eq. (11) with respect to density, constant speed of sound for the liquid and mixture is found for water: $c_l = 1482.35 m/s$ and $c_m = 1 m/s$, following Brennen [68] and Örley et al. [151]. For the ideal gas, the speed of sound is calculated from:

$$c_g = \sqrt{R_g T_{ref}}, \quad (13)$$

In the three phase mixture, the speed of sound between lm and g phases is determined by the Wallis speed of sound [68, 156]:

$$\frac{1}{\rho c^2} = \frac{1 - \beta_g}{\rho_{lm} c_{lm}^2} + \frac{\beta_g}{\rho_g c_g^2}, \quad (14)$$

505 In order to calculate the pressure of the mixture, a closed form equation of state describing the co-existence of three phases is employed from Eq. (6):

$$\rho = \beta_{lm} \left[\rho_{l,sat} + \frac{1}{c^2} (p - p_{sat}) \right] + \beta_g \frac{p}{R_g T_{ref}}, \quad (15)$$

replacing the volume fraction β_g from Eq. (7) and eliminating β_{lm} by using Eq. (9) and Eq. (12), a quadratic equation for the pressure is derived:

$$Ap^2 + Bp + C = 0, \quad (16)$$

where

$$A = \frac{1}{c^2}, \quad (17)$$

$$B = \rho(Y_g - 1) + \rho_{l,sat} - \frac{p}{c^2} - \frac{Y_g \rho R_g T_{ref}}{c^2}, \quad (18)$$

$$C = Y_g \rho R_g T_{ref} \left(\frac{p_{sat}}{c^2} - \rho_{l,sat} \right). \quad (19)$$

510 In the case of two real solutions $p_1, p_2 \in \mathbb{R}$, the largest root of Eq. (16) is kept. The speed of sound in Eq. (17), (18) and (19) is set to either c_l or c_m , depending on the pressure at the previous time step for identifying the liquid or mixture regions. Therefore, Eq. (16) is solved iteratively, in case the computed pressure does not fulfil the original assumption. In practice, the algorithm is
515 repeated for no more than three iterations.

3.4. Discretization

Due to the large variation in the speed of sound, the Mach number in three phase flows can range from 10^{-2} up to 10^2 or even higher [157]. As it can be seen in the previous sub-section from Eq. (13) and (11), the speed of sound
520 can vary from 1 m/s in the mixture regime, up to 1482.35 m/s in the liquid region, whereas in the gaseous phase the speed of sound is 290 m/s . This is an obstacle in density-based solvers, since they are prone to slow convergence and

dispersion in low Mach number flows [158, 159, 160]. In order to handle the low Mach number problem, a hybrid flux, suitable for multiphase flows, is proposed
 525 here for first time.

The aforementioned flux is based on the Primitive Variable Riemann Solver (PVRS) [161] and the Mach consistent numerical flux of Schmidt et al. [162]. That way, an efficient and robust solver is developed, by utilizing an approximated Riemann solver, instead of the exact one. At the same time, the numerical
 530 scheme is suitable for subsonic up to supersonic flow conditions. The numerical inviscid flux in the k direction at the $i + 1/2$ interface takes the following form:

$$\mathbf{F}_k^{i+1/2} = \rho^{L/R} u_k^* \begin{bmatrix} 1 \\ Y_g^{L/R} \\ u_1^{L/R} \\ u_2^{L/R} \\ u_3^{L/R} \end{bmatrix} + p^* \begin{bmatrix} 0 \\ 0 \\ \delta_{1k} \\ \delta_{2k} \\ \delta_{3k} \end{bmatrix}, \quad (20)$$

where the interface velocity u_k^* is approximated by:

$$u_k^* = \frac{1}{C^L + C^R} [C^L u_k^L + C^R u_k^R + (p^L - p^R)], \quad (21)$$

and C is the acoustic impedance $C = \rho c$. The interface pressure p^* is:

$$p^* = (1 - \beta)p^{*,incr} + \beta p^{*,comp}. \quad (22)$$

In Eq. (22), the interface pressure is the sum of the incompressible and the
 535 compressible parts, where the incompressible contribution is:

$$p^{*,incr} = \frac{C^L p^R + C^R p^L}{C^L + C^R}, \quad (23)$$

and the compressible contribution is:

$$p^{*,comp} = \frac{C^L p^R + C^R p^L + C^R C^L (u_k^L - u_k^R)}{C^L + C^R} \quad (24)$$

Depending on the Mach number, the contribution of the incompressible or the compressible part in Eq. (22) is more dominant and the weighted term β is :

$$\beta = 1 - e^{-\alpha M}, \quad (25)$$

where the Mach number M is defined as:

$$M = \max\left(\frac{|\mathbf{u}^L|}{c^L}, \frac{|\mathbf{u}^R|}{c^R}\right). \quad (26)$$

540 The blending coefficient is $\alpha \sim (10, 100)$. For incompressible single phase flow, Eq. (23) is taking the form of $\frac{1}{2}(p_L + p_R)$ since $C^L = C^R$. However, for two-phase flows, Eq. (23) is much closer to the exact solution.

Linear interpolation (2nd order spatial accuracy) with van Leer flux limiter has been used [163]. A four stage Runge-Kutta (RK), 4th order accurate in
545 time has been implemented for time advancement [161], in order to capture the waves which are propagating in the domain.

4. Results

In this section, verification and validation of the numerical method is performed; then, the effect of various impact velocities on a 2-D axisymmetric
550 droplet impact is investigated. The Riemann problem is chosen for verifying the algorithm accuracy and demonstrating its ability to resolve wave dynamics. Possible difficulties of the numerical scheme, which is prone to numerical diffusion and dispersion, especially at the phase boundaries are also investigated. The 2-D planar droplet impact case is then selected for qualitative validation
555 of the propagating shock and the reflected expansion waves against available experimental data. Finally, the 2-D axisymmetric droplet impingement on a solid wall is modelled for different impact velocities, in order to investigate the extent of the cavitation zone and how bubble collapse can possibly lead to material erosion. The droplet impact simulations are summarised in Table 1, where
560 the Reynolds, Weber and Froude numbers are calculated.

Table 1: Numbering, description, impact velocity, Reynolds, Weber and Froude numbers of the droplet impact cases which have been simulated. As wedge are denoted the 2-D axisymmetric simulations and no air means that in the initial condition the droplet is attached to the wall, in comparison to the rest of the simulations where the droplet is 3 cells above the wall in the beginning of the simulation.

Name	Description	u_{imp} (m/s)	Re	We	Fr
1	planar 2-D	110	$1.1 \cdot 10^6$	$1.67 \cdot 10^6$	351.2
2	wedge	110	$1.1 \cdot 10^6$	$1.67 \cdot 10^6$	351.2
3	wedge	27.5	$2.75 \cdot 10^5$	$1.05 \cdot 10^5$	87.8
4	wedge	55	$5.5 \cdot 10^5$	$4.19 \cdot 10^5$	175.6
5	wedge	82.5	$8.2 \cdot 10^5$	$9.43 \cdot 10^5$	263.4
6	wedge	220	$2.2 \cdot 10^6$	$6.71 \cdot 10^6$	702.4
7	wedge	550	$5.5 \cdot 10^6$	$4.19 \cdot 10^7$	1756
8	wedge, no air	27.5	$2.75 \cdot 10^5$	$1.05 \cdot 10^5$	87.8

4.1. Riemann Problem

The first benchmark case is the Riemann problem in the computational domain $x \in [-0.5, 0.5]$ with initial conditions for the left state: $\rho_L = 998.2 \text{ kg/m}^3$, $u_L = 0 \text{ m/s}$, $Y_g = 0$ and for the right state: $\rho_R = 0.017 \text{ kg/m}^3$, $u_R = 0 \text{ m/s}$, $Y_g = 1$. Wave transmissive boundary conditions have been used for the left and the right sides of the shock tube, that is $\mathbf{U}_{n+1}(x = L) = \mathbf{U}_n(x = L)$ and $\mathbf{U}_{n+1}(x = 0) = \mathbf{U}_n(x = 0)$. A CFL number of 0.5 was chosen for the time step selection in the explicit algorithm. Comparison between the exact and the numerical solution is shown in Fig. 1 at time $t = 0.1 \mu\text{s}$, where second order of spatial accuracy with 500 equally spaced cells in the x direction was used for obtaining the numerical solution. A close-up view in order to compare first and second order in space schemes with resolution either 500 or 1000 equally spaced cells in the x direction is shown in Fig. 2. In Fig. 1, the exact solution of the Riemann problem and the computed one are in satisfactory agreement and the wave pattern has been correctly captured. As it was expected in Fig. 2, the 2nd order solutions in space have minimal numerical diffusion, which is dominant

in the 1st order schemes. In addition, the computed solution is getting closer to the exact by increasing the mesh resolution and the numerical diffusion is eliminated. No dispersion is noticed at the boundary interface (between the gas and the liquid), which is the case when using conventional schemes such as HLLC or similar. The exact solution of the Riemann problem is not trivial for multi-material cases and it has been derived following the Appendix A of the present paper.

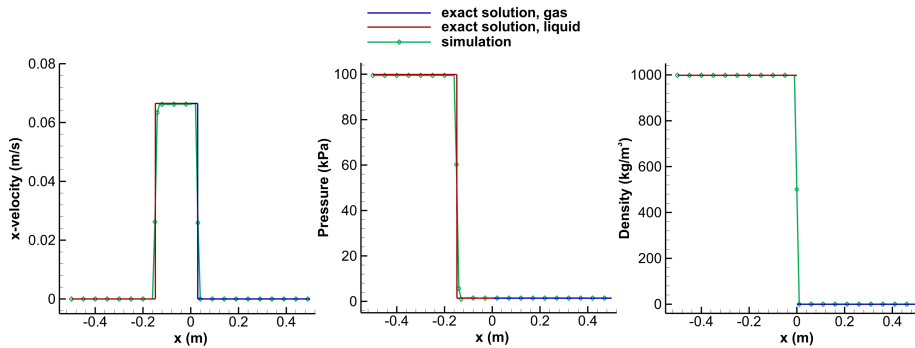


Figure 1: Verification of the two-phase solver in the Riemann problem. Comparison of the x-velocity (left), pressure (middle) and density (right) between the exact and the numerical solution at time $t = 0.1 \mu s$. Second order accuracy in space with 500 cells has been used.

4.2. Planar droplet impact

The second test case examined is a planar 'droplet' impact on a solid wall for which experimental data are available [1]. A 2-D simulation, with second order discretization in space was performed in order to validate the algorithm against the 2-D experimental data of Field at al. [1]. A circular cross-section water column of $D = 10 mm$ in diameter is placed between two transparent plates, separated by a small distance. The impact is modelled by a third plate which is projected with velocity $110 m/s$ among the two plates. For the numerical simulation, the centre of the droplet was placed at $(x_0, y_0) = (0, 0.00505) m$ in the computational domain $(-0.2, 0.2) \times (0, 0.2) m$; 150 cells have been placed along the initial droplet radius R (grid size $\sim 33 \mu m$). The same cell size as in

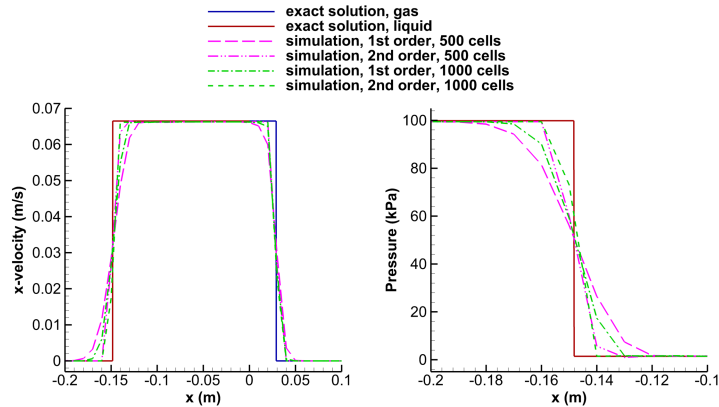


Figure 2: Close-up view of the Riemann problem. Comparison of the x-velocity (left) and pressure (left) between the exact and the numerical solution at time $t = 0.1 \mu s$. First and second order spatial accuracy schemes with resolution of 500 and 1000 cells have been used.

595 the droplet radius has been kept until distance $2R$ in the positive and negative x-direction and until $1.5R$ in the positive y-direction. After that, a stretching ratio of 1.05 has been applied, resulting in a total amount of $380 k$ cells. A CFL number of 0.5 was chosen for the time step selection ($\Delta t \sim 5 \cdot 10^{-9} s$) in the explicit algorithm. Initially, the pressure of the surrounding air and the water droplet is atmospheric, $p(t = 0) = 101326 Pa$. In this way, the initial density for the two phases is calculated from the barotropic EoS: $\rho_l(t = 0) = 998.207 kg/m^3$ and $\rho_g(t = 0) = 1.204 kg/m^3$. Zero gradient boundary conditions have been selected for the right, left and upper faces, whereas the lower face is set as wall.

600 In Fig. 3 the experiment [1] (left) and the numerical solution (right) for the droplet impact are compared.

605

The main mechanisms noticed both in the experimental work [10, 1] and past numerical simulations [146, 148, 149] are jetting, as well as shock and expansion waves; these are also identified in the present study. In the aforementioned compressible numerical studies, cavitation was not modelled and different impact conditions were simulated compared to the present work. In frame (a) the droplet impacts the wall, whereas in the next frame, a shock wave is forming, as a result of the impact. While the liquid close to the impact point is compressed,

the information of the impact has not travelled in the rest of the droplet, which is still moving with the impact velocity [144]. Those two regions are separated
 615 by the shock front (frame (b)), which is created by individual wavelets emanating from the contact edge [145, 10]. In the preliminary stages of the impact, the edge velocity is higher than the speed of sound and there is a tendency to decrease. As long as the edge velocity is higher than the shock speed, the shock is attached to the contact edge. When the edge velocity reaches the critical value
 620 of the shock speed, the shock wave is detached from the contact line (frame (c)) and it is propagating in the rest of the liquid (until frame (g)). This mechanism is responsible for the expansion of the liquid and the jetting, which is created in the contact edge (frame (d) , denoted as J in the experimental results). In frames (e) , (f) and (g) , the shock wave is reflected normal to the free surface
 625 as an expansion wave which focuses in the inner region of the drop. These low pressure areas are potential cavitation regimes and their extent, as well as the volume of the vapour depend on the impact velocity [149]. In frames (g) , (h) , the shock wave reaches the highest point of the drop and it is then reflected downwards. In the last frames, the jetting is more advanced and the reflected
 630 shock is shown in the upper middle of the drop at frames (i) and (j) (denoted as R in frame (i) and focused to point F in frame (j) of the experiment).

Comparing the present simulation with previous experimental studies of Field et al. [1], similar wave structures at the same time scale are noticed. The edge pressure in the contact edge is around 0.22 GPa and it exceeds the water
 635 hammer pressure [10], which is estimated about 0.16 GPa , where the water hammer pressure is defined as $p_{wh} = \rho_l c_l u_{imp}$. The shock wave moving upwards and its reflection have been recognized at similar time frames between the experiment and the simulation. Furthermore, the jetting (starting from frame (d)) is around ten times the impact speed, or even higher, as it has been mentioned
 640 in [10]. Rarefaction waves have been also identified in the later stages of the droplet impact and they follow the same pattern as in the experimental study. The production of vapour in the final stages is evident due to the pressure drop and the areas where vapour is generated are in accordance to the experiment.

However, in the experimental study the maximum volume of vapour is in the
 645 centre of the droplet, whereas in the present work, vapour is more dominant
 on the upper sides, perimetrically of the droplet. This is because bulk liquid
 tension cannot be captured with the present methodology.

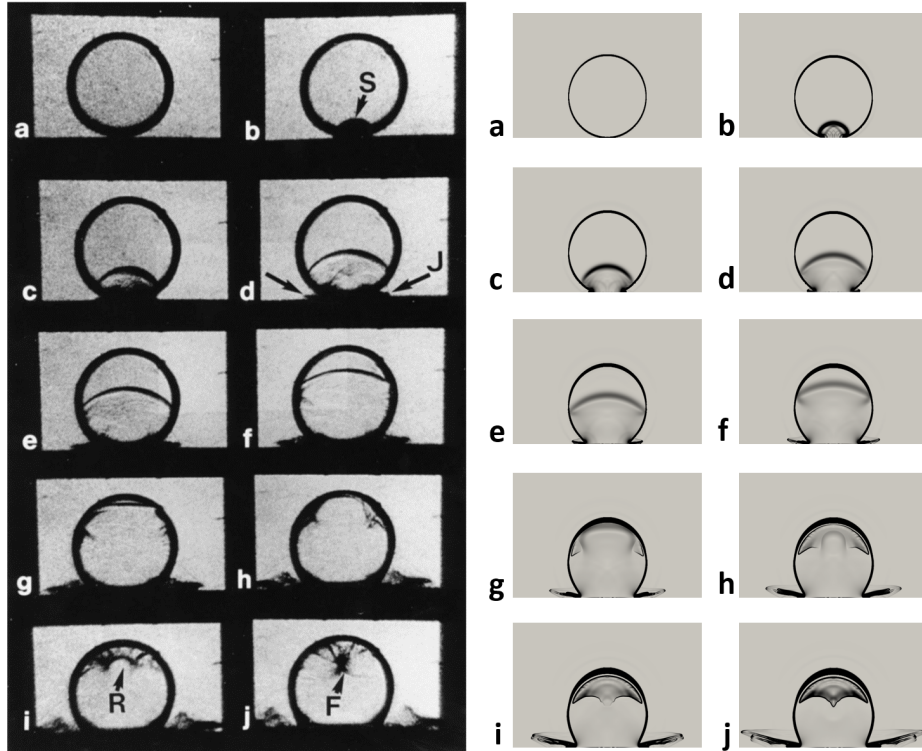


Figure 3: Validation of the numerical solution (right) against experiment (left) for a 2-D drop impact on a solid wall with impact velocity 110 m/s . The interframe time is $t = 1\ \mu\text{s}$. The left figure is taken from Field et. al [1].

4.3. 2-D axisymmetric droplet impact

The previous simulation is now performed in a 2-D axisymmetric computa-
 650 tional domain, in order to model the impact of spherical droplets. A 3-D simula-
 tion would generally had captured the 3-D interfacial instabilities due to surface
 tension, but since the We number is above 10^5 and in order to reduce the compu-
 tational cost, a 2-D axisymmetric simulation is performed instead. The droplet

impact time scale is $t_{impact} = D/u_{imp}$ and in the present configuration for im-
 655 pact velocity $u_{imp} = 110\text{ m/s}$ is calculated to be $t_{impact} \approx 9 \cdot 10^{-5}\text{ s}$, whereas
 the cavitation collapse time is approximated from the characteristic Rayleigh
 time $t_{cav} = 0.915R_{0,vap}\sqrt{\frac{\rho_l}{p_{\infty}-p_{sat}}}$ and it is calculated to be $t_{cav} \approx 2.2 \cdot 10^{-5}\text{ s}$.
 Starting from the half of the 2-D meshes of 4.2, a wedge of 5 degrees has been
 simulated by taking advantage of the axial symmetry. The same initial and
 660 boundary conditions are kept, apart from the wedge faces and the axis of sym-
 metry. At the beginning, a grid independence analysis is performed and then,
 the effect of the impact velocity's magnitude is investigated for the intermediate
 grid. Second order accurate spatial discretization schemes have been used for
 this simulation and a CFL number of 0.5 was chosen for the time step selection
 665 ($\Delta t \sim 3 \cdot 10^{-10}\text{ s}$) in the explicit algorithm. In the following figures, pressure
 has been non-dimensionalized with the water hammer pressure p_{wh} , velocity
 with the impact velocity u_{imp} and the dimensionless time is calculated from:
 $t = \frac{T-t_{bimp}}{D/c_l}$, where $t_{bimp} = 0.00005/u_{imp}$ is the time of the impact, based on
 the initial configuration (in cases where the droplet is not attached to the wall,
 670 but there is air between them). This way, the shock wave will be at the same
 y-position at a given non-dimensional time for all impact velocities.

In Fig. 4 the results of the grid independence study are shown having as
 impact velocity 110 m/s . Three different grids have been utilized, with 117 k ,
 380 k and 1.5 M cells. In the fine area: $(0, 2R) \times (0, 1.5R)$ the resolution of
 675 330×225 , 660×450 and 1320×900 cells has been used for the three different
 grids. On the left-hand side of Fig. 4, the maximum wall pressure with respect
 to time is shown and on the right-hand side the generated volume of vapour
 at a line parallel to the y axis ($x = 0.6\text{ mm}$) at time $t = 1.19$ is plotted. The
 maximum wall pressures are similar for all grids and the peak noticed in the
 vapour volume fraction after $y = 0.8$ is almost identical for all resolutions. It
 680 can be concluded from the above study that there is convergence of the solution
 for the selected grid resolutions. The intermediate grid (380 k cells), referred as
case 2 from now on, is considered to be accurate enough and it is selected for
 the rest of the simulations.

685 In Fig. 5 and 6 the evolution of the droplet impact is shown for *case 2*. More
 specifically, in Fig. 5 the pressure field (left slice) and the velocity magnitude
 (right slice) are shown in conjunction with the iso-surface of 0.5 gas mass frac-
 tion on the left figures, whereas on the right figures, the numerical Schlieren is
 depicted by utilizing different scales for the inner and the outer computational
 690 domain of the droplet in order to capture the different waves, which are propa-
 gating in the liquid water and in the air. In Fig. 6 the wall pressure (lower slice)
 and the vapour volume fraction (upper slice) combined with the iso-surface of
 0.5 gas mass fraction are demonstrated for *case 2*. The main mechanisms and
 the flow pattern in the 2-D axisymmetric simulation (*case 2*) are similar to the
 695 planar one (*case 1*) for the same impact velocity (110 m/s). At time $t = 0.44$
 the droplet has already impacted the wall and the shock wave is visible in the
 Schlieren figure. The jetting has started, however it is more evident at time
 $t = 0.89$ and it is responsible for the non-spherical shape of the droplet. As
 the shock moves to the upper half of the droplet, it is reflected on the droplet
 700 surface and expansion waves, which are moving downwards, are noticed in the
 Schlieren figures, starting from time $t = 0.89$. Those rarefaction waves create
 low pressure areas and thus, cavitation is noticed at times $t = 1.19$ and $t = 1.48$
 (see also Fig. 6). The maximum wall pressure is realised at the moment of the
 impact and it decreases afterwards (see Fig. 11).

705 The planar and the axisymmetric solutions exhibit many similarities; nev-
 ertheless, there is a discrepancy in the pressure field between *case 1* and *case*
2. The maximum wall pressure is higher in *case 1*, as it can be seen in Fig. 7
 and has been also noticed in previous studies [10]. In *case 1* the shock wave
 propagates in a cylindrical pattern and it is reflected on the upper half surface
 710 of the cylinder, whereas in *case 2* the shock wave travels in a spherical pattern
 and it is reflected on the upper surface of the spherical droplet. The three-
 dimensionality of the latter results in a shock wave of the half pressure strength
 ($\sim 10\text{ MPa}$), compared to the planar case ($\sim 20\text{ MPa}$).

In Fig. 8, the above results are compared to lower impact velocities, 55 m/s
 715 and 27.5 m/s at the same dimensionless time $t = 1.48$. The same configuration

as in the left image of Fig. 5 is followed here as well. The droplet spreading at lower impact speeds is less dominant and the droplet is closer to the spherical shape, as it can be seen from the droplet iso-surface plots. On the other hand, in *case 2* the transition to splashing is evident, as the jetting area is split to two different regions. Furthermore, the high pressure area and the lamella are larger in *case 2* but the ratio $|\mathbf{u}_{max}|/u_{imp}$ in all cases (*case 2-4*) is between 7.2 and 11, whereas the ratio p_{max}/p_{wh} is around 0.13. Although the above indicate similar non-dimensional maximum pressures and jetting velocities regardless the impact velocity, it is worth pointing out that the maximum pressure and velocity fields are significantly lower in *case 3* and *4*. For example, the jetting velocity is reduced by even one order of magnitude (~ 1400 m/s in *case 2* and ~ 190 m/s in *case 4*).

In order to compare the vapour generated for each impact velocity at the same non dimensional time $t = 1.48$, slices with the vapour volume contour (upper) combined with the same iso-surface are shown in Fig. 9 for *case 2, 3* and *4*. For the highest impact velocity (*case 2*) the vapour volume is increased even one order of magnitude compared to the values of lower velocities. It can be concluded that the amount of the vapour and the extent of the cavitation area, which is generated at later stages, monotonically depends on the impact velocity (this is also evident in Fig. 11 where 6 different impact velocities are examined). The wall pressure (bottom) is also depicted in Fig. 9; although the maximum is approximately the same for all cases, it extends to a larger area for higher impact velocities.

At a later stage of the droplet impact (Fig. 10), the splashing is more evident than at time $t = 1.48$. In Fig. 10 the pressure field (left slice) and the velocity magnitude (right slice) are shown in conjunction with the iso-surface of 0.5 gas mass fraction on the left figures, whereas on the right figures the wall pressure (lower slice) and the vapour volume fraction (upper slice) combined with the iso-surface of 0.5 gas mass fraction are demonstrated for *case 2*. Several vaporous regions have been created from the rarefaction waves and they start collapsing consecutively. At times $t = 3.19$ and $t = 3.56$ the third and second vaporous

regions have just collapsed respectively. A peak in the pressure due to the shock wave created by the collapse is noticed at times $t = 3.56$ and $t = 3.64$, however the location (far away from the wall) and the strength (maximum pressure is $0.09p_{wh}$) cannot denote erosion.

In Fig. 11 a parametric study for six different impact velocities (*case 2-7*) is performed for the intermediate grid resolution, where the maximum wall pressure (left) and the generated volume of vapour (right) with respect to time are plotted. As it has been already discussed in the previous paragraph and in previous studies [7, 149], it is straightforward that higher impact velocities result in higher wall pressures (although the ratio $\frac{p_{max,wall}}{p_{wh}}$ is almost constant regardless of the impact velocity). More production of vapour due to the reflection of a stronger shock developing during the liquid-solid contact is calculated. The cavitation inside the droplet may also contribute to pressure increase on the solid surface at the bubble collapse stage. This is shown on the wall pressure figure, where at higher impact velocities there are small peaks occurring at later times (*case 7*).

It is remarkable that the initial configuration can affect the existence or not of cavitation and material erosion close to the wall, even for low impact velocities. As initial condition in *case 8* is now selected the droplet to be attached to the wall (in contrast to *case 1-7*), so there is no air between them. To demonstrate that the impact velocity is not the determining factor here, $u_{imp} = 27.5 m/s$ was selected. Surprisingly enough, in Fig. 12 vapour is created at the impact point and a vaporous region is formed above it due to a rarefaction wave at an early stage of the impact. The maximum vapour volume fraction created is even three times higher than *case 2* at time $t = 1.48$, where the impact velocity is four times larger. Consequently, there is a significant increase in the pressure field due to the collapse, as it can be observed in Fig. 13, which results in around 60% higher wall pressure, compared to *case 3*. In practice, the above case can be realised at steam turbine blades, where the rarefied environment implies very low steam density, consequently there is little droplet/vapour interaction.

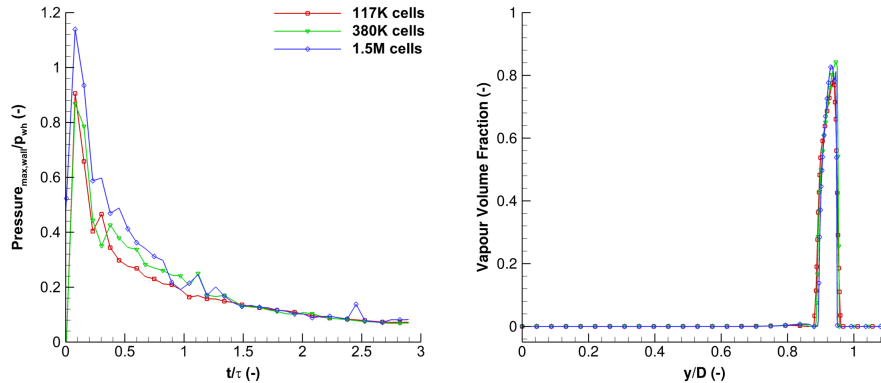


Figure 4: Grid independence study for three different grids (coarse, intermediate, fine). Maximum wall pressure with respect to time is shown on the left. The values of the vapour volume fraction on the right figure are exported at a line parallel to the y axis starting from $x = 0.6 \text{ mm}$, $z = 0$ at time $T = 0.083$. Wall pressure is divided by p_{wh} , time is measured from the moment of the impact and it is non-dimensionalized with $\tau = D/c_l$, whereas distance y has been divided by the drop diameter D .

5. Conclusions

In the present work, the impact of droplets onto solid surfaces at conditions inducing cavitation within its volume have been addressed. Initially, a literature review on the subject has been given, focusing primarily on computational studies. It is apparent that the vast majority of them assume incompressible liquids and aim to resolve the temporal development of the droplet/gas interface. Some studies also aim to consider the heat transfer and phase-change phenomena induced during impact at elevated wall temperature. Under such conditions, wettability effects and contact angle play a dominant role to the impact outcome, with vast literature reporting relevant findings. However, more relevant to the present study are the conditions at high impact velocities where liquid compressibility becomes important. For conditions inducing cavitation within the droplet's volume, only one set of experiments is reported in the literature while no computational study has been performed so far. Aiming to provide further inside to this problem, an explicit density-based solver of the

Euler equations, able to model gaseous, liquid and vapour phases has been developed in OpenFOAM. Moreover, a Mach number consistent numerical flux, capable of handling a wide range of Mach number flows and producing smooth solutions at the phase boundaries has been proposed. The main model assumptions and simplifications have been justified for the flow conditions of interest to the present study. The developed algorithm was then validated against the Riemann problem, followed by the comparison against the 2-D planar 'droplet' impact experiment, showing satisfactory agreement, as similar flow patterns have been identified. Following, simulation of the impact of spherical droplets on a solid surface have been performed, including for the first time the simulation of cavitation formation and collapse. These cavitation regimes are formed by the reflection of the shock wave on the outer surface of the droplet as an expansion wave.

The droplet impact time scale is $t_{impact} = D/u_{imp}$ and in the present configuration for impact velocity $u_{imp} = 110\text{ m/s}$ is calculated to be $t_{impact} \approx 9 \cdot 10^{-5}\text{ s}$, whereas the cavitation collapse time is approximated from the characteristic Rayleigh time $t_{cav} = 0.915R_{0,vap}\sqrt{\frac{\rho_l}{p_\infty - p_{sat}}}$ and it is calculated to be $t_{cav} \approx 2.2 \cdot 10^{-5}\text{ s}$. The significantly larger time scale ($t_{impact} \approx 9 \cdot 10^{-5}\text{ s}$) of the droplet impact phenomenon in comparison to the characteristic time of the cavitation collapse ($t_{cav} \approx 2.2 \cdot 10^{-5}\text{ s}$) justifies why the collapse of the vaporous regions inside the droplet don't affect the shape of the droplet and its splashing.

The impact velocity strongly affects the droplet shape and spreading, as well as the jetting velocity and the volume of vapour produced in the upper area of the droplet. Increased impact velocity may result in more damage and possibly material erosion not only because of higher impact pressure, but also due to the collapse of the vaporous bubbles inside the droplet. However, in order to notice significant pressure increase due to the bubble collapse, the impact velocity must be extremely high which is rather difficult to be realised in practical applications such as steam turbines. Apart from that, the initial location of the droplet with respect to the solid surface, which actually means the absence or not of gas around the droplet, can influence the volume of cavitation generated at the

initial stages of the impact. If there is no gas between the droplet and the solid surface, pressure can get close to its maximum value, which is at the moment of the impact (p_{wh}) and material erosion may take place ($p_{wh} = 160 MPa$ for $u_{imp} = 110 m/s$ and the yield strength of steel is $200 - 300 MPa$). It should be clarified here that the above phenomenon can even occur at low impact velocities, for instance at impact velocity $u_{imp} = 27.5 m/s$.

Acknowledgements

The research leading to these results has received funding from the MSCA-ITN-ETN of the European Union's H2020 programme, under REA grant agreement n. 642536. The authors would also like to acknowledge the contribution of The Lloyd's Register Foundation. Lloyd's Register Foundation helps to protect life and property by supporting engineering-related education, public engagement and the application of research.

Appendix A. Exact Riemann problem for multi-material problems

In this section, the methodology for finding the exact solution to the Riemann problem for the multi-material Euler equations is derived. In the literature there are limited works discussing exact Riemann solvers for multi-material applications. Mainly, these focus on multiple velocities, pressures and temperature fields, see e.g. [164, 165]. The discussion here will be limited to just two different materials sharing the same velocity, pressure and temperature fields. The materials will be referred to as *material-1* and *material-2*, however the methodology may be extended to any number of materials. For the sake of generality, the discussion will not be limited to an explicit form of equation of state. Instead, the equations of state for the two distinct materials will be assumed to depend on density and internal energy only, i.e. have a form $p = p(\rho)$ or $p = p(\rho, e)$, which may have an explicit formula or be in tabular form as in [166, 128]. Material variation will be tracked using a mass fraction transport equation which will affect the mixture equation of state. Thus, the mixture equation of state

that will be examined is of the form $p = p(\rho, Y)$ or $p = p(\rho, e, Y)$, where Y is the mass fraction of *material-2*, defined in Eq. (9). Following Toro [161], the form of the Riemann problem solved is:

$$\begin{cases} \frac{\partial \mathbf{U}}{\partial t} + \frac{\partial \mathbf{F}(\mathbf{U})}{\partial x} = 0 \\ \mathbf{U}(x, 0) = \begin{cases} \mathbf{U}_L, & \mathbf{x} < \mathbf{0} \\ \mathbf{U}_R, & \mathbf{x} \geq \mathbf{0} \end{cases} \end{cases} \quad (\text{A.1})$$

The same nomenclature as in the rest of the paper is used.

855 *Appendix A.1. Pressure is only a function of density and mass fraction*

In case the mixture pressure is only a function of density and mass fraction, $p = p(\rho, Y)$ the conservative variables and the flux vector are:

$$\mathbf{U} = \begin{bmatrix} \rho \\ \rho u \\ \rho Y \end{bmatrix}, \quad \mathbf{F}(\mathbf{U}) = \begin{bmatrix} \rho u \\ \rho u^2 + p \\ \rho u Y \end{bmatrix}, \quad (\text{A.2})$$

To derive the Jacobian matrix, it is convenient to recast the \mathbf{U} and $\mathbf{F}(\mathbf{U})$ vectors and equation of state $p = p(\rho, Y)$, as:

$$\mathbf{U} = \begin{bmatrix} u_1 \\ u_2 \\ u_3 \end{bmatrix}, \quad \mathbf{F}(\mathbf{U}) = \begin{bmatrix} u_2 \\ \frac{u_2^2}{u_1} + p\left(u_1, \frac{u_3}{u_1}\right) \\ \frac{u_3 u_2}{u_1} \end{bmatrix}, \quad (\text{A.3})$$

$$p = p\left(u_1, \frac{u_3}{u_1}\right) \quad (\text{A.4})$$

860 The Jacobian matrix is calculated as:

$$\mathbf{A}(\mathbf{U}) = \begin{bmatrix} \frac{\partial f_1}{\partial u_1} & \frac{\partial f_1}{\partial u_2} & \frac{\partial f_1}{\partial u_3} \\ \frac{\partial f_2}{\partial u_1} & \frac{\partial f_2}{\partial u_2} & \frac{\partial f_2}{\partial u_3} \\ \frac{\partial f_3}{\partial u_1} & \frac{\partial f_3}{\partial u_2} & \frac{\partial f_3}{\partial u_3} \end{bmatrix} \quad (\text{A.5})$$

After calculating all terms and replacing back the conservative variables:

$$\mathbf{A}(\mathbf{U}) = \begin{bmatrix} 0 & 1 & 0 \\ \frac{\partial p}{\partial \rho} - u^2 - \frac{\partial p}{\partial Y} \frac{Y}{\rho} & 2u & \frac{1}{\rho} \frac{\partial p}{\partial Y} \\ -uY & Y & u \end{bmatrix} \quad (\text{A.6})$$

The eigenvalue analysis of the Jacobian matrix results to:

$$\begin{aligned} \lambda_1 &= u - c \\ \lambda_2 &= u \\ \lambda_3 &= u + c \end{aligned} \quad (\text{A.7})$$

and right eigenvectors:

$$\mathbf{K}_1 = \begin{bmatrix} 1 \\ u - c \\ Y \end{bmatrix}, \quad \mathbf{K}_2 = \begin{bmatrix} \frac{\partial p}{\partial Y} \\ u \frac{\partial p}{\partial Y} \\ Y \frac{\partial p}{\partial Y} - \rho \frac{\partial p}{\partial \rho} \end{bmatrix}, \quad \mathbf{K}_3 = \begin{bmatrix} 1 \\ u + c \\ Y \end{bmatrix} \quad (\text{A.8})$$

where c is the speed of sound equal to $\sqrt{\frac{\partial p}{\partial \rho}}$. The waves associated with λ_1 , λ_3
 865 eigenvalues are non-linear waves (shock waves or rarefaction waves) and the λ_2
 eigenvalue is a linearly degenerate wave associated with a contact discontinuity.

Appendix A.2. Pressure is a function of density, internal energy and mass fraction

In case the mixture pressure is only a function of density, internal energy and mass fraction, $p = p(\rho, e, Y)$ the conservative variables and the flux vector are:

$$\mathbf{U} = \begin{bmatrix} \rho \\ \rho u \\ \rho E \\ \rho Y \end{bmatrix}, \quad \mathbf{F}(\mathbf{U}) = \begin{bmatrix} \rho u \\ \rho u^2 + p \\ u(\rho E + p) \\ \rho u Y \end{bmatrix}, \quad (\text{A.9})$$

where $E = 1/2u^2 + e$, with e the internal energy. To derive the Jacobian matrix, it is convenient to recast the \mathbf{U} and $\mathbf{F}(\mathbf{U})$ vectors and EoS $p = p(\rho, e, Y)$ as:

$$\mathbf{U} = \begin{bmatrix} u_1 \\ u_2 \\ u_3 \\ u_4 \end{bmatrix}, \quad \mathbf{F}(\mathbf{U}) = \begin{bmatrix} u_2 \\ \frac{u_2^2}{u_1} + p\left(u_1, \frac{u_3}{u_1} - \frac{u_2^2}{2u_1}, \frac{u_4}{u_1}\right) \\ \frac{u_2}{u_1} \left(u_3 + p\left(u_1, \frac{u_3}{u_1} - \frac{u_2^2}{2u_1}, \frac{u_4}{u_1}\right) \right) \\ \frac{u_4 u_2}{u_1} \end{bmatrix}, \quad (\text{A.10})$$

$$p = p\left(u_1, \frac{u_3}{u_1} - \frac{u_2^2}{2u_1}, \frac{u_4}{u_1}\right) \quad (\text{A.11})$$

The Jacobian matrix is:

$$\mathbf{A}(\mathbf{U}) = \begin{bmatrix} 0 & & & \\ \frac{2\frac{\partial p}{\partial \rho}\rho + \frac{\partial p}{\partial e}(u^2 - 2e) - 2\left(\rho u^2 + \frac{\partial p}{\partial Y}Y\right)}{2\rho} & & & \\ u\left(\frac{-\frac{\partial p}{\partial e}u^2 + \rho u^2 + 2\frac{\partial p}{\partial e}e + 2p - 2\rho\frac{\partial p}{\partial \rho} + 2e\rho + 2Y\frac{\partial p}{\partial Y}}{2\rho}\right) & & & \\ -uY & & & \\ & 1 & 0 & 0 \\ & \left(2 - \frac{\partial p}{\partial e}\frac{1}{\rho}\right)u & \frac{\partial p}{\partial e}\frac{1}{\rho} & \frac{\partial p}{\partial Y}\frac{1}{\rho} \\ & \frac{\left(\rho - 2\frac{\partial p}{\partial e}\right)u^2 + 2p + 2e\rho}{2\rho} & \frac{u}{\rho}\left(\frac{\partial p}{\partial e} + \rho\right) & \frac{u}{\rho}\frac{\partial p}{\partial Y} \\ & Y & 0 & u \end{bmatrix} \quad (\text{A.12})$$

The Jacobian eigenvalues $[\lambda_1, \lambda_2, \lambda_3, \lambda_4]$ are:

$$\begin{aligned}
\lambda_1 &= u - c \\
\lambda_2 &= \lambda_3 = u \\
\lambda_4 &= u + c
\end{aligned} \quad (\text{A.13})$$

875 and right eigenvectors:

$$\begin{aligned}
 \mathbf{K}_1 &= \begin{bmatrix} 1 \\ u - c \\ \frac{1}{2}(u^2 - cu + 2p/\rho + 2e) \\ Y \end{bmatrix}, & \mathbf{K}_2 &= \begin{bmatrix} 2\frac{1}{X}\frac{\partial p}{\partial Y} \\ 2\frac{u}{X}\frac{\partial p}{\partial Y} \\ 0 \\ 1 \end{bmatrix}, \\
 \mathbf{K}_3 &= \begin{bmatrix} 2\frac{1}{X}\frac{\partial p}{\partial e} \\ 2\frac{u}{X}\frac{\partial p}{\partial e} \\ 1 \\ 0 \end{bmatrix}, & \mathbf{K}_4 &= \begin{bmatrix} 1 \\ u + c \\ \frac{1}{2}(u^2 + cu + 2p/\rho + 2e) \\ Y \end{bmatrix}
 \end{aligned} \tag{A.14}$$

where c is the speed of sound, defined as: $c = \sqrt{\frac{\partial p}{\partial \rho} + \frac{\partial p}{\partial e} \frac{p}{\rho^2}}$ and $X = \frac{\partial p}{\partial e} u^2 + 2\frac{\partial p}{\partial e} e - 2\frac{\partial p}{\partial \rho} \rho + 2\frac{\partial p}{\partial Y} Y$.

The waves associated with λ_1, λ_4 eigenvalues are non-linear waves (shock waves or rarefaction waves) and the λ_2, λ_3 eigenvalues are linearly degenerate waves associated with a contact discontinuity.

Appendix A.3. Exact solver derivation

Despite the difference in the Jacobian matrix structure with respect to the single material, ideal gas Euler equations [161], the eigenstructure is very similar. In both cases (pressure is function of ρ, Y or pressure is a function of ρ, e, Y), the eigenvalues correspond to two non-linear waves and one contract discontinuity wave. In fact, since the material interface will travel at the contact discontinuity, allows to split the original multi-material Riemann problem, to two coupled single-material Riemann problems, as shown in Fig. A.14 and A.15.

Consequently, to solve the multi-material Riemann problem exactly, one has to do the following procedure:

- Assume an initial star region velocity, u^* .

- Based on this assumed u^* , solve each material separately, with a single material Riemann solver, assuming that the contact discontinuity is a moving wall at velocity $u_{wall} = u^*$. General Riemann solvers for arbitrary equations of state in the form of $p = p(\rho)$ or $p = p(\rho, e)$ may be found in [128].
 895 The solution of each single-material problem is done assuming wall boundary conditions, i.e. $p_R = p_L$, $\rho_R = \rho_L$, but $u_R = -u_L + 2u_{wall}$. For example, in Fig. A.15, when solving for *material-1*, the right state conditions are $\mathbf{U} = \begin{bmatrix} \rho_L & \rho_L(2u_{wall} - u_L) & e_L \end{bmatrix}^T$. Similarly for *material-2*, the left state conditions are $\mathbf{U} = \begin{bmatrix} \rho_R & \rho_R(2u_{wall} - u_R) & e_R \end{bmatrix}^T$.
 900

- After solving the two individual Riemann problems for *material-1* and *material-2*, the calculated star region pressure for the two materials p_1^* and p_2^* is not necessarily the same. Thus, the u^* velocity must be corrected iteratively, until $p_1^* = p_2^*$.

- Once $p_1^* = p_2^*$ up to a prescribed tolerance, the exact solution of the Riemann problem is the superposition of the two individual problems, i.e. the L and L^* states from *material-1* and R and R^* states from *material-2*. Note that in cases of large disparities in the acoustic impedance of the materials (e.g. liquid/gas interfaces), p^* will be very sensitive to small variations of u^* for the stiff phase, thus under-relaxation of the corrected u^* is advised.
 910

As a demonstration of the aforementioned solver, the following cases will be examined and compared with PVRS solvers in literature [161]. The material properties are as follows:

material-1: Liquid EoS, $p = c_L^2(\rho - \rho_{l,sat}) + p_{sat}$, $c_L = 1482.35 \text{ m/s}$, $p_{sat} =$
 915 2340 Pa , $\rho_{l,sat} = 998.16 \text{ kg/m}^3$

material-2: Gas EoS, $p = \rho R_g T_{ref}$, $R_g = 287.06 \text{ J/(kgK)}$, $T_{ref} = 293 \text{ K}$

Appendix A.3.1. Case A

The initial configuration of the Riemann problem is shown in Table A.2. The exact solution is $p^* = 1430.9 \text{ Pa}$ and $u^* = 0.067 \text{ m/s}$. The PVRS-solver, using
 920 average states between L , R fails to properly predict the star region; in fact, it

predicts $p^* = 50666.7 Pa$ (3440.9 % deviation from exact) and $u^* = 0.11 m/s$ (66.9 % deviation from exact). On the other hand, the PVRS-solver outlined in section 3.4, predicts $p^* = 1430.9 Pa$ (practically identical to exact solution) and $u^* = 0.066 m/s$ (0.2 % deviation from exact). Note that this is the same case used for validation in section 4.1.

Table A.2: Initial configuration for the Riemann problem of Appendix A.3.1.

<i>material-1</i> , $x < 0$ (Liquid)	<i>material-2</i> , $x \geq 0$ (Gas)
$\rho_L = 998.202 kg/m^3$	$\rho_R = 0.017 kg/m^3$
$u_L = 0 m/s$	$u_R = 0 m/s$
$p_L = 99902.8 Pa$	$p_R = 1400 Pa$

Appendix A.3.2. Case B

The second Riemann problem is a much more demanding case, since there is a huge pressure and density variation between the L , R states. The initial configuration of this Riemann problem is shown in Table A.3. The exact solution is $p^* = 144.4 Pa$ and $u^* = 2.73 m/s$. The PVRS-solver, using average states between L , R again fails to properly predict the star region, due to the averaging; in fact, it predicts $p^* = 20.2 \cdot 10^5 Pa$ (1400000 % deviation from exact) and $u^* = 4.56 m/s$ (66.7 % deviation from exact). On the other hand, the PVRS-solver outlined in section 3.4, predicts $p^* = 144.4 Pa$ (practically identical to exact solution) and $u^* = 2.72 m/s$ (0.32 % deviation from exact).

Table A.3: Initial configuration for the Riemann problem of Appendix A.3.2.

<i>material-1</i> , $x < 0$ (Liquid)	<i>material-2</i> , $x \geq 0$ (Gas)
$\rho_L = 1000 kg/m^3$	$\rho_R = 0.0017 kg/m^3$
$u_L = 0 m/s$	$u_R = 0 m/s$
$p_L = 40.4 \cdot 10^5 Pa$	$p_R = 143 Pa$

Appendix A.3.3. Case C

In this case, although the pressure and density ratios are much lower than the case in section Appendix A.3.2, the challenge is to predict the induced depressurization due to the high gas velocity. The initial configuration of this Riemann problem is shown in Table A.4. The exact solution is $p^* = 81548 Pa$ and $u^* = 2.68 m/s$. The PVRS-solver, using average states between L, R again fails catastrophically, predicting a negative p^* ; it predicts $p^* = -154923 Pa$ (290 % deviation from exact) and $u^* = 9.46 m/s$ (250 % deviation from exact). On the other hand, the PVRS-solver outlined in section 3.4, predicts $p^* = 82025 Pa$ (0.59 % deviation from exact solution) and $u^* = 2.67 m/s$ (0.33 % deviation from exact).

Table A.4: Initial configuration for the Riemann problem of Appendix A.3.3.

<i>material-1</i> , $x < 0$ (Liquid)	<i>material-2</i> , $x \geq 0$ (Gas)
$\rho_L = 1000 kg/m^3$	$\rho_R = 1 kg/m^3$
$u_L = 0 m/s$	$u_R = 10 m/s$
$p_L = 40.4 \cdot 10^5 Pa$	$p_R = 84151 Pa$

Appendix A.3.4. Case D

Also, in order to demonstrate the capability in predicting temperature effects and taking into account energy equation, a case examined by Saurel et al. [165] will be discussed. This case involves interaction of vapour and liquid dodecane, modelled as ideal gas and stiffened gas respectively. The properties of the materials are:

material-1: Liquid, stiffened gas EoS, $p = e(\gamma_L - 1)\rho - \gamma_L p_\infty$, $e = c_{v,L}T + \frac{p_\infty}{\rho}$, $c_{v,L} = 1077 J/(kgK)$, $p_\infty = 4 \cdot 10^8 Pa$, $\gamma_L = 2.35$

material-2: Ideal gas EoS, $p = \rho R_g T_{ref}$, $e = c_{v,G}T$, $R_g = 48.9 J/(kgK)$, $c_{v,G} = 1956 J/(kgK)$

The initial discontinuity in this case is described in Table A.5. The exact solution with the described solver is $p^* = 186835.8 kg/m^3$, $u^* = 140.7 m/s$, $\rho_{*,L} =$

454.9 kg/m^3 , $\rho_{\star,R} = 3.68 \text{ kg/m}^3$ which is identical with the published solution.

Table A.5: Initial configuration for the Riemann problem of Appendix A.3.3.

<i>material-1</i> , $x < 0$ (Liquid)	<i>material-2</i> , $x \geq 0$ (Gas)
$\rho_L = 500 \text{ kg/m}^3$	$\rho_R = 2 \text{ kg/m}^3$
$u_L = 0 \text{ m/s}$	$u_R = 0 \text{ m/s}$
$p_L = 10^8 \text{ Pa}$	$p_R = 10^5 \text{ Pa}$
$T_L = 688 \text{ K}$	$T_R = 1022.3 \text{ K}$

960 **Appendix B. Isentropic Compression**

In Table B.6, isentropic compression of liquid water starting from saturation conditions ($T = 293 \text{ K}$, $p = 2317 \text{ Pa}$) is calculated based on the properties of [167, 168]. The temperature increase is negligible for pressure 2500 bar ($\sim 6 \text{ K}$) and even for higher pressures, temperature increase is not significant in comparison to the other phenomena which take place. For example, in the previous
965 droplet simulations for impact velocity 110 m/s , the maximum pressure is 1460 bar resulting in temperature increase less than 3.5 K . The above justify the barotropic EoS which was selected and the omission of thermal effects.

Table B.6: Temperature difference for isentropic compression of liquid water. Properties are derived from [167].

Pressure (Pa)	Temperature (K)	Temperature Difference (K)
2317.45	293	0
10^7	293.15	0.15
10^8	294.959	1.959
$2.5 \cdot 10^8$	299.109	6.109
$5 \cdot 10^8$	306.905	13.905
10^9	321.933	28.933

References

- 970 [1] J. Field, J.-J. Camus, M. Tinguely, D. Obreschkow, M. Farhat,
Cavitation in impacted drops and jets and the effect on erosion
damage thresholds, *Wear* 290291 (2012) 154 – 160. doi:<http://doi.org/10.1016/j.wear.2012.03.006>.
URL <http://www.sciencedirect.com/science/article/pii/S0043164812000968>
- 975
- [2] M. Rein, Phenomena of liquid drop impact on solid and liquid surfaces,
Fluid Dynamics Research 12 (1993) 61–93. doi:10.1016/0169-5983(93)
90106-K.
- [3] A. Yarin, Drop impact dynamics: Splashing, spreading, receding,
bouncing, *Annual Review of Fluid Mechanics* 38 (1) (2006) 159–
980 192. arXiv:<http://dx.doi.org/10.1146/annurev.fluid.38.050304.092144>, doi:10.1146/annurev.fluid.38.050304.092144.
URL <http://dx.doi.org/10.1146/annurev.fluid.38.050304.092144>
- [4] R. I. Crane, Droplet deposition in steam turbines, *Proceedings of the*
985 *Institution of Mechanical Engineers, Part C: Journal of Mechanical Engineering Science* 218 (8) (2004) 859–870. arXiv:<http://dx.doi.org/10.1243/0954406041474200>, doi:10.1243/0954406041474200.
URL <http://dx.doi.org/10.1243/0954406041474200>
- [5] R. Andrade, O. Skurtys, F. Osorio, Drop impact behavior on
990 food using spray coating: Fundamentals and applications, *Food Research International* 54 (1) (2013) 397 – 405. doi:<https://doi.org/10.1016/j.foodres.2013.07.042>.
URL <http://www.sciencedirect.com/science/article/pii/S0963996913004080>
- 995 [6] G. D. Martin, S. D. Hoath, I. M. Hutchings, Inkjet printing - the physics of
manipulating liquid jets and drops, *Journal of Physics: Conference Series*

105 (1) (2008) 012001.

URL <http://stacks.iop.org/1742-6596/105/i=1/a=012001>

1000 [7] J. Fukai, Z. Zhao, D. Poulikakos, C. M. Megaridis, O. Miyatake, Modeling of the deformation of a liquid droplet impinging upon a flat surface, *Physics of Fluids A: Fluid Dynamics* 5 (11) (1993) 2588–2599. [arXiv: http://dx.doi.org/10.1063/1.858724](https://arxiv.org/abs/199305001), [doi:10.1063/1.858724](https://doi.org/10.1063/1.858724).

URL <http://dx.doi.org/10.1063/1.858724>

1005 [8] Y. Guo, Y. Lian, M. Sussman, Investigation of drop impact on dry and wet surfaces with consideration of surrounding air, *Physics of Fluids* 28 (7) (2016) 073303. [arXiv: http://aip.scitation.org/doi/pdf/10.1063/1.4958694](https://arxiv.org/abs/160503001), [doi:10.1063/1.4958694](https://doi.org/10.1063/1.4958694).

URL <http://aip.scitation.org/doi/abs/10.1063/1.4958694>

1010 [9] Q. Zhou, N. Li, X. Chen, A. Yonezu, T. Xu, S. Hui, D. Zhang, Water drop erosion on turbine blades: Numerical framework and applications, *MATERIALS TRANSACTIONS* 49 (7) (2008) 1606–1615. [doi:10.2320/matertrans.MRA2008025](https://doi.org/10.2320/matertrans.MRA2008025).

1015 [10] J. E. Field, M. B. Lesser, J. P. Dear, Studies of two-dimensional liquid-wedge impact and their relevance to liquid-drop impact problems, *Proceedings of the Royal Society of London A: Mathematical, Physical and Engineering Sciences* 401 (1821) (1985) 225–249. [doi:10.1098/rspa.1985.0096](https://doi.org/10.1098/rspa.1985.0096).

URL <http://rspa.royalsocietypublishing.org/content/401/1821/225>

1020 [11] J. E. Field, J. P. Dear, J. E. Ogren, The effects of target compliance on liquid drop impact, *Journal of Applied Physics* 65 (2) (1989) 533–540. [arXiv: http://dx.doi.org/10.1063/1.343136](https://arxiv.org/abs/198902001), [doi:10.1063/1.343136](https://doi.org/10.1063/1.343136).

URL <http://dx.doi.org/10.1063/1.343136>

1025 [12] F. H. Harlow, J. P. Shannon, The splash of a liquid drop, *Journal of Applied Physics* 38 (10) (1967) 3855–3866. [arXiv: http://dx.doi.org/](https://arxiv.org/abs/196710001)

10.1063/1.1709031, doi:10.1063/1.1709031.

URL <http://dx.doi.org/10.1063/1.1709031>

1030 [13] C. Hirt, B. Nichols, Volume of fluid (vof) method for the dynamics of free boundaries, *Journal of Computational Physics* 39 (1) (1981) 201 – 225. doi:[http://dx.doi.org/10.1016/0021-9991\(81\)90145-5](http://dx.doi.org/10.1016/0021-9991(81)90145-5).

URL <http://www.sciencedirect.com/science/article/pii/S0021999181901455>

[14] D. L. Youngs, An interface tracking method for a 3d eulerian hydrodynamics code, Technical report 44/92/35, AWRE (1984).

1035 [15] M. Rudman, Volume-tracking methods for interfacial flow calculations, *International Journal for Numerical Methods in Fluids* 24 (7) (1997) 671–691. doi:10.1002/(SICI)1097-0363(19970415)24:7<671::AID-FLD508>3.0.CO;2-9.

URL [http://dx.doi.org/10.1002/\(SICI\)1097-0363\(19970415\)24:7<671::AID-FLD508>3.0.CO;2-9](http://dx.doi.org/10.1002/(SICI)1097-0363(19970415)24:7<671::AID-FLD508>3.0.CO;2-9)

1040 [16] W. Aniszewski, T. Mnard, M. Marek, Volume of fluid (vof) type advection methods in two-phase flow: A comparative study, *Computers & Fluids* 97 (2014) 52 – 73. doi:<https://doi.org/10.1016/j.compfluid.2014.03.027>.

1045 URL <http://www.sciencedirect.com/science/article/pii/S0045793014001261>

[17] J. Fukai, Y. Shiiba, T. Yamamoto, O. Miyatake, D. Poulikakos, C. M. Megaridis, Z. Zhao, Wetting effects on the spreading of a liquid droplet colliding with a flat surface: Experiment and modeling, *Physics of Fluids* 7 (2) (1995) 236–247. arXiv:<https://doi.org/10.1063/1.868622>, doi:10.1063/1.868622.

1050 URL <https://doi.org/10.1063/1.868622>

[18] M. Francois, W. Shyy, Computations of drop dynamics with the immersed boundary method, part 2: Drop impact and heat transfer, *Numerical Heat*

- 1055 Transfer, Part B: Fundamentals 44 (2) (2003) 119–143. arXiv:<https://doi.org/10.1080/713836348>, doi:10.1080/713836348.
URL <https://doi.org/10.1080/713836348>
- [19] . ikalo, H.-D. Wilhelm, I. V. Roisman, S. Jakirli, C. Tropea, Dynamic
contact angle of spreading droplets: Experiments and simulations, Physics
1060 of Fluids 17 (6) (2005) 062103. arXiv:<https://doi.org/10.1063/1.1928828>, doi:10.1063/1.1928828.
URL <https://doi.org/10.1063/1.1928828>
- [20] S. Mitra, M. J. Sathe, E. Doroodchi, R. Utikar, M. K. Shah, V. Pareek,
J. B. Joshi, G. M. Evans, Droplet impact dynamics on a spherical particle,
1065 Chemical Engineering Science 100 (2013) 105 – 119, 11th International
Conference on Gas-Liquid and Gas-Liquid-Solid Reactor Engineering.
doi:<https://doi.org/10.1016/j.ces.2013.01.037>.
URL [http://www.sciencedirect.com/science/article/pii/
S000925091300050X](http://www.sciencedirect.com/science/article/pii/S000925091300050X)
- 1070 [21] M. Pasandideh-Fard, S. Aziz, S. Chandra, J. Mostaghimi, Cooling
effectiveness of a water drop impinging on a hot surface, Interna-
tional Journal of Heat and Fluid Flow 22 (2) (2001) 201 – 210.
doi:[https://doi.org/10.1016/S0142-727X\(00\)00086-2](https://doi.org/10.1016/S0142-727X(00)00086-2).
URL [http://www.sciencedirect.com/science/article/pii/
S0142727X00000862](http://www.sciencedirect.com/science/article/pii/S0142727X00000862)
- 1075 [22] M. Bussmann, J. Mostaghimi, S. Chandra, On a three-dimensional volume
tracking model of droplet impact, Physics of Fluids 11 (6) (1999) 1406–
1417. arXiv:<http://dx.doi.org/10.1063/1.870005>, doi:10.1063/1.
870005.
1080 URL <http://dx.doi.org/10.1063/1.870005>
- [23] I. Roisman, L. Opfer, C. Tropea, M. Raessi, J. Mostaghimi,
S. Chandra, Drop impact onto a dry surface: Role of the dy-
namic contact angle, Colloids and Surfaces A: Physicochemical

- and Engineering Aspects 322 (1) (2008) 183 – 191. doi:<https://doi.org/10.1016/j.colsurfa.2008.03.005>.
1085 URL <http://www.sciencedirect.com/science/article/pii/S0927775708001738>
- [24] M. Marengo, C. Antonini, I. V. Roisman, C. Tropea, Drop
collisions with simple and complex surfaces, Current Opin-
1090 ion in Colloid & Interface Science 16 (4) (2011) 292 – 302.
doi:<https://doi.org/10.1016/j.cocis.2011.06.009>.
URL <http://www.sciencedirect.com/science/article/pii/S1359029411000859>
- [25] A. M. Ardekani, S. Dabiri, R. H. Rangel, Deformation of a droplet in a
1095 particulate shear flow, Physics of Fluids 21 (9) (2009) 093302. arXiv:
<https://doi.org/10.1063/1.3205446>, doi:10.1063/1.3205446.
URL <https://doi.org/10.1063/1.3205446>
- [26] I. Malgarinos, N. Nikolopoulos, M. Gavaises, Numerical in-
1100 vestigation of heavy fuel droplet-particle collisions in the in-
jection zone of a fluid catalytic cracking reactor, part ii: 3d
simulations, Fuel Processing Technology 156 (2017) 43 – 53.
doi:<https://doi.org/10.1016/j.fuproc.2016.09.012>.
URL <http://www.sciencedirect.com/science/article/pii/S0378382016305136>
- [27] B. J. Parker, D. L. Youngs, Two and three dimensional eulerian simula-
1105 tion of fluid flow with material interfaces, Technical report, UK Atomic
Weapons Establishment, Aldermaston, Berkshire (01/1992).
- [28] R. Scardovelli, S. Zaleski, Direct numerical simulation of free-surface
and interfacial flow, Annual Review of Fluid Mechanics 31 (1) (1999)
1110 567–603. arXiv:<https://doi.org/10.1146/annurev.fluid.31.1.567>,
doi:10.1146/annurev.fluid.31.1.567.
URL <https://doi.org/10.1146/annurev.fluid.31.1.567>

- [29] K. Yokoi, Efficient implementation of {THINC} scheme: A simple and practical smoothed {VOF} algorithm, *Journal of Computational Physics* 226 (2) (2007) 1985 – 2002. doi:<https://doi.org/10.1016/j.jcp.2007.06.020>.
URL <http://www.sciencedirect.com/science/article/pii/S0021999107002732>
- [30] M. Marek, W. Aniszewski, A. Boguslawski, Simplified volume of fluid method (svof) for two-phase flows., *TASK Quaterly* 12 (2008) 25565.
- [31] F. Xiao, Y. Honma, T. Kono, A simple algebraic interface capturing scheme using hyperbolic tangent function, *International Journal for Numerical Methods in Fluids* 48 (9) (2005) 1023–1040. doi:10.1002/flid.975.
URL <http://dx.doi.org/10.1002/flid.975>
- [32] D. P. Garrick, W. A. Hagen, J. D. Regele, An interface capturing scheme for modeling atomization in compressible flows, *Journal of Computational Physics* (2017) –doi:<https://doi.org/10.1016/j.jcp.2017.04.079>.
URL <http://www.sciencedirect.com/science/article/pii/S0021999117303674>
- [33] F. Xiao, S. Ii, C. Chen, Revisit to the {THINC} scheme: A simple algebraic {VOF} algorithm, *Journal of Computational Physics* 230 (19) (2011) 7086 – 7092. doi:<https://doi.org/10.1016/j.jcp.2011.06.012>.
URL <http://www.sciencedirect.com/science/article/pii/S0021999111003615>
- [34] R. K. Shukla, C. Pantano, J. B. Freund, An interface capturing method for the simulation of multi-phase compressible flows, *Journal of Computational Physics* 229 (19) (2010) 7411 – 7439. doi:<https://doi.org/10.1016/j.jcp.2010.06.025>.
URL <http://www.sciencedirect.com/science/article/pii/S0021999110003402>

- [35] M. L. Norman, K.-H. A. Winkler, 2-D Eulerian Hydrodynamics with Fluid Interfaces, Self-Gravity and Rotation, Springer Netherlands, Dordrecht, 1986, pp. 187–221. doi:10.1007/978-94-009-4754-2_6.
1145 URL http://dx.doi.org/10.1007/978-94-009-4754-2_6
- [36] E. Puckett, J. Saltzman, A 3d adaptive mesh refinement algorithm for multimaterial gas dynamics, *Physica D: Nonlinear Phenomena* 60 (1) (1992) 84 – 93. doi:[http://dx.doi.org/10.1016/0167-2789\(92\)90228-F](http://dx.doi.org/10.1016/0167-2789(92)90228-F).
1150 URL <http://www.sciencedirect.com/science/article/pii/S016727899290228F>
- [37] G. H. Miller, E. G. Puckett, A high-order godunov method for multiple condensed phases, *Journal of Computational Physics* 128 (1) (1996) 134 – 164. doi:<http://dx.doi.org/10.1006/jcph.1996.0200>.
1155 URL <http://www.sciencedirect.com/science/article/pii/S0021999196902004>
- [38] R. Saurel, R. Abgrall, A simple method for compressible multifluid flows, *SIAM Journal on Scientific Computing* 21 (3) (1999) 1115–1145. arXiv:<http://dx.doi.org/10.1137/S1064827597323749>, doi:10.1137/S1064827597323749.
1160 URL <http://dx.doi.org/10.1137/S1064827597323749>
- [39] J. Roenby, H. Bredmose, H. Jasak, A computational method for sharp interface advection, *Royal Society Open Science* 3 (11). doi:10.1098/rsos.160405.
1165 URL <http://rsos.royalsocietypublishing.org/content/3/11/160405>
- [40] T. Maric, H. Marschall, D. Bothe, vofoam - a geometrical volume of fluid algorithm on arbitrary unstructured meshes with local dynamic adaptive mesh refinement using openfoam arXiv:1305.3417v1.

- 1170 [41] S. Popinet, Gerris: a tree-based adaptive solver for the in-
compressible euler equations in complex geometries, *Journal of*
Computational Physics 190 (2) (2003) 572 – 600. doi:[https://doi.org/10.1016/S0021-9991\(03\)00298-5](https://doi.org/10.1016/S0021-9991(03)00298-5).
URL <http://www.sciencedirect.com/science/article/pii/S0021999103002985>
- 1175
- [42] D. Fuster, G. Agbaglah, C. Josserand, S. Popinet, S. Zaleski, Numerical
simulation of droplets, bubbles and waves: state of the art, *Fluid Dynam-*
ics Research 41 (6) (2009) 065001.
URL <http://stacks.iop.org/1873-7005/41/i=6/a=065001>
- [43] H. Jadidbonab, N. Mitroglou, I. Karathanassis, M. Gavaises, Experi-
mental study of diesel-fuel droplet impact on a similarly sized polished
spherical heated solid particle, *Langmuir* 34 (1) (2018) 36–49, pMID:
29172533. arXiv:<https://doi.org/10.1021/acs.langmuir.7b01658>,
doi:10.1021/acs.langmuir.7b01658,
1180 URL <https://doi.org/10.1021/acs.langmuir.7b01658>
- 1185
- [44] R. Rioboo, C. Tropea, M. Marengo, Outcomes from a drop impact on
solid surfaces, *Atomization and Sprays* 11 (2).
- [45] A. A. Saha, S. K. Mitra, Effect of dynamic contact angle in a
volume of fluid (vof) model for a microfluidic capillary flow, *Jour-*
nal of Colloid and Interface Science 339 (2) (2009) 461 – 480.
1190 doi:<https://doi.org/10.1016/j.jcis.2009.07.071>.
URL <http://www.sciencedirect.com/science/article/pii/S0021979709010297>
- [46] Y. Sui, H. Ding, P. D. Spelt, Numerical simulations of flows with moving
contact lines, *Annual Review of Fluid Mechanics* 46 (1) (2014) 97–119.
1195 arXiv:<https://doi.org/10.1146/annurev-fluid-010313-141338>,
doi:10.1146/annurev-fluid-010313-141338.
URL <https://doi.org/10.1146/annurev-fluid-010313-141338>

- [47] M. Shirota, M. A. J. van Limbeek, C. Sun, A. Prosperetti, D. Lohse,
1200 Dynamic leidenfrost effect: Relevant time and length scales, *Phys. Rev. Lett.* 116 (2016) 064501. doi:[10.1103/PhysRevLett.116.064501](https://doi.org/10.1103/PhysRevLett.116.064501).
URL <https://link.aps.org/doi/10.1103/PhysRevLett.116.064501>
- [48] V. Bertola, An impact regime map for water drops impacting on heated
surfaces, *International Journal of Heat and Mass Transfer* 85 (2015) 430
1205 – 437. doi:<https://doi.org/10.1016/j.ijheatmasstransfer.2015.01.084>.
URL <http://www.sciencedirect.com/science/article/pii/S0017931015000927>
- [49] G. Liang, S. Shen, Y. Guo, J. Zhang, Boiling from liquid drops impact on
1210 a heated wall, *International Journal of Heat and Mass Transfer* 100 (2016)
48 – 57. doi:<https://doi.org/10.1016/j.ijheatmasstransfer.2016.04.061>.
URL <http://www.sciencedirect.com/science/article/pii/S0017931016306548>
- [50] U. Vengateson, R. Mohan, Experimental and modeling study of
1215 fluidized bed granulation: Effect of binder flow rate and flu-
idizing air velocity, *Resource-Efficient Technologies* 2 (2016)
S124 – S135, special Issue on Technoscape-2016. doi:<https://doi.org/10.1016/j.refit.2016.10.003>.
1220 URL <http://www.sciencedirect.com/science/article/pii/S2405653716300987>
- [51] M. Renksizbulut, R. Haywood, Transient droplet evaporation with
variable properties and internal circulation at intermediate reynolds
numbers, *International Journal of Multiphase Flow* 14 (2) (1988) 189 –
1225 202. doi:[https://doi.org/10.1016/0301-9322\(88\)90005-5](https://doi.org/10.1016/0301-9322(88)90005-5).
URL <http://www.sciencedirect.com/science/article/pii/S0301932288900055>

- 1230 [52] C. M. MEGARIDIS, W. A. SIRIGNANO, Multicomponent droplet vaporization in a laminar convective environment, *Combustion Science and Technology* 87 (1-6) (1993) 27–44. arXiv:<https://doi.org/10.1080/00102209208947205>, doi:10.1080/00102209208947205.
URL <https://doi.org/10.1080/00102209208947205>
- 1235 [53] H. Zhang, Evaporation of a suspended droplet in forced convective high-pressure environments, *Combustion Science and Technology* 175 (12) (2003) 2237–2268. arXiv:<https://doi.org/10.1080/714923282>, doi:10.1080/714923282.
URL <https://doi.org/10.1080/714923282>
- 1240 [54] G. Strotos, M. Gavaises, A. Theodorakakos, G. Bergeles, Numerical investigation on the evaporation of droplets depositing on heated surfaces at low weber numbers, *International Journal of Heat and Mass Transfer* 51 (7) (2008) 1516 – 1529. doi:<https://doi.org/10.1016/j.ijheatmasstransfer.2007.07.045>.
URL <http://www.sciencedirect.com/science/article/pii/S0017931007005066>
- 1245 [55] M. Gumulya, R. P. Utikar, V. Pareek, R. Mead-Hunter, S. Mitra, G. M. Evans, Evaporation of a droplet on a heated spherical particle, *Tailoring Sustainability through Chemical Reaction Engineering* 278 (2015) 309–319.
URL <http://www.sciencedirect.com/science/article/pii/S1385894714014673>
- 1250 [56] D. J. Harvie, D. F. Fletcher, A hydrodynamic and thermodynamic simulation of droplet impacts on hot surfaces, part ii: validation and applications, *International Journal of Heat and Mass Transfer* 44 (14) (2001) 2643 – 2659. doi:[https://doi.org/10.1016/S0017-9310\(00\)00304-5](https://doi.org/10.1016/S0017-9310(00)00304-5).
URL <http://www.sciencedirect.com/science/article/pii/S0017931000003045>

- [57] S. Tonini, G. Cossali, A multi-component drop evaporation model based on analytical solution of stefanmaxwell equations, *International Journal of Heat and Mass Transfer* 92 (2016) 184 – 189. doi:<https://doi.org/10.1016/j.ijheatmasstransfer.2015.08.014>.
1260 URL <http://www.sciencedirect.com/science/article/pii/S0017931015301551>
- [58] V. Zubkov, G. Cossali, S. Tonini, O. Rybdylova, C. Crua, M. Heikal, S. Sazhin, Mathematical modelling of heating and evaporation of a spheroidal droplet, *International Journal of Heat and Mass Transfer* 108 (2017) 2181 – 2190. doi:<https://doi.org/10.1016/j.ijheatmasstransfer.2016.12.074>.
1265 URL <http://www.sciencedirect.com/science/article/pii/S001793101633438X>
- [59] S. Tonini, G. Cossali, On molar- and mass-based approaches to single component drop evaporation modelling, *International Communications in Heat and Mass Transfer* 77 (2016) 87 – 93. doi:<https://doi.org/10.1016/j.icheatmasstransfer.2016.06.014>.
1270 URL <http://www.sciencedirect.com/science/article/pii/S0735193316302068>
1275
- [60] J. Breitenbach, I. V. Roisman, C. Tropea, Drop collision with a hot, dry solid substrate: Heat transfer during nucleate boiling, *Phys. Rev. Fluids* 2 (2017) 074301. doi:[10.1103/PhysRevFluids.2.074301](https://doi.org/10.1103/PhysRevFluids.2.074301).
URL <https://link.aps.org/doi/10.1103/PhysRevFluids.2.074301>
- [61] J. Breitenbach, I. V. Roisman, C. Tropea, Heat transfer in the film boiling regime: Single drop impact and spray cooling, *International Journal of Heat and Mass Transfer* 110 (Complete) (2017) 34–42. doi:[10.1016/j.ijheatmasstransfer.2017.03.004](https://doi.org/10.1016/j.ijheatmasstransfer.2017.03.004).
1280
- [62] M. PasandidehFard, Y. M. Qiao, S. Chandra, J. Mostaghimi, Capillary effects during droplet impact on a solid surface, *Physics of Fluids*
1285

8 (3) (1996) 650–659. arXiv:<http://dx.doi.org/10.1063/1.868850>,
doi:10.1063/1.868850.

URL <http://dx.doi.org/10.1063/1.868850>

1290 [63] M. PasandidehFard, S. Chandra, J. Mostaghimi, A three-dimensional
model of droplet impact and solidification, International Jour-
nal of Heat and Mass Transfer 45 (11) (2002) 2229 – 2242.
doi:[https://doi.org/10.1016/S0017-9310\(01\)00336-2](https://doi.org/10.1016/S0017-9310(01)00336-2).
URL [http://www.sciencedirect.com/science/article/pii/
S0017931001003362](http://www.sciencedirect.com/science/article/pii/S0017931001003362)

1295 [64] M. Rieber, A. Frohn, A numerical study on the mechanism of splashing,
International Journal of Heat and Fluid Flow 20 (5) (1999) 455 – 461.
doi:[https://doi.org/10.1016/S0142-727X\(99\)00033-8](https://doi.org/10.1016/S0142-727X(99)00033-8).
URL [http://www.sciencedirect.com/science/article/pii/
S0142727X99000338](http://www.sciencedirect.com/science/article/pii/S0142727X99000338)

1300 [65] I. Malgarinos, N. Nikolopoulos, M. Marengo, C. Antonini, M. Gavaises,
Vof simulations of the contact angle dynamics during the drop
spreading: Standard models and a new wetting force model,
Advances in Colloid and Interface Science 212 (2014) 1 – 20.
doi:<http://dx.doi.org/10.1016/j.cis.2014.07.004>.
1305 URL [http://www.sciencedirect.com/science/article/pii/
S0001868614002280](http://www.sciencedirect.com/science/article/pii/S0001868614002280)

[66] K. Ling, W.-Q. Tao, Numerical simulation of nucleate boiling in shallow
liquid, Computers & Fluids 164 (2018) 35 – 40, special Issue devoted to
The Asian Symposium on Computational Heat Transfer and Fluid Flow
1310 2015 (ASCHT 2015) held in Busan, Korean on November 22-25, 2015.
doi:<https://doi.org/10.1016/j.compfluid.2016.12.026>.
URL [http://www.sciencedirect.com/science/article/pii/
S0045793016304145](http://www.sciencedirect.com/science/article/pii/S0045793016304145)

- [67] P. H. Streng, A. Orell, J. W. Westwater, Microscopic study of bubble growth during nucleate boiling, *AICHE Journal* 7 (4) 578–583. 1315
arXiv:<https://onlinelibrary.wiley.com/doi/pdf/10.1002/aic.690070410>, doi:10.1002/aic.690070410.
URL <https://onlinelibrary.wiley.com/doi/abs/10.1002/aic.690070410>
- [68] E. Brennen C., *Cavitation and Bubble Dynamics*, 1995. 1320
- [69] A. Moita, A. Moreira, Drop impacts onto cold and heated rigid surfaces: Morphological comparisons, disintegration limits and secondary atomization, *International Journal of Heat and Fluid Flow* 28 (4) (2007) 735 – 752, including Special Issue of Conference on Modelling Fluid Flow (CMFF06), Budapest. 1325
doi:<https://doi.org/10.1016/j.ijheatfluidflow.2006.10.004>.
URL <http://www.sciencedirect.com/science/article/pii/S0142727X06001706>
- [70] A. Moita, A. Moreira, Influence of surface properties on the dynamic behavior of impacting droplets. 1330
- [71] M. Bussmann, S. Chandra, J. Mostaghimi, Modeling the splash of a droplet impacting a solid surface, *Physics of Fluids* 12 (12) (2000) 3121–3132. arXiv:<https://doi.org/10.1063/1.1321258>, doi:10.1063/1.1321258. 1335
URL <https://doi.org/10.1063/1.1321258>
- [72] P. R. Gunjal, V. V. Ranade, R. V. Chaudhari, Dynamics of drop impact on solid surface: Experiments and vof simulations, *AICHE Journal* 51 (1) 59–78. arXiv:<https://onlinelibrary.wiley.com/doi/pdf/10.1002/aic.10300>, doi:10.1002/aic.10300. 1340
URL <https://onlinelibrary.wiley.com/doi/abs/10.1002/aic.10300>

- [73] J. Brackbill, D. Kothe, C. Zemach, A continuum method for modeling surface tension, *Journal of Computational Physics* 100 (2) (1992) 335 – 354. doi:[http://dx.doi.org/10.1016/0021-9991\(92\)90240-Y](http://dx.doi.org/10.1016/0021-9991(92)90240-Y).
1345 URL <http://www.sciencedirect.com/science/article/pii/S002199919290240Y>
- [74] S. Kistler, *Hydrodynamics of wetting. Wettability*, New York, 1993.
- [75] Y. Shikhmurzaev, *Capillary flows with forming interfaces*.
- [76] C. Antonini, F. J. Carmona, E. Pierce, M. Marengo, A. Amirfazli,
1350 General methodology for evaluating the adhesion force of drops and bubbles on solid surfaces, *Langmuir* 25 (11) (2009) 6143–6154, PMID: 19408902. arXiv:<https://doi.org/10.1021/la804099z>, doi:10.1021/la804099z.
URL <https://doi.org/10.1021/la804099z>
- [77] . ikalo, E. Gani, Phenomena of dropletsurface interactions, *Experimental Thermal and Fluid Science* 31 (2) (2006) 97 – 110, second International Thermal Science Seminar (ITSS II). doi:<https://doi.org/10.1016/j.expthermflusci.2006.03.028>.
1355 URL <http://www.sciencedirect.com/science/article/pii/S0894177706000434>
1360
- [78] C.-D. Wu, L.-M. Kuo, S.-J. Lin, T.-H. Fang, S.-F. Hsieh, Effects of temperature, size of water droplets, and surface roughness on nanowetting properties investigated using molecular dynamics simulation, *Computational Materials Science* 53 (1) (2012) 25 – 30.
1365 doi:<https://doi.org/10.1016/j.commatsci.2011.09.024>.
URL <http://www.sciencedirect.com/science/article/pii/S0927025611005325>
- [79] M. S. Plesset, R. B. Chapman, Collapse of an initially spherical vapour cavity in the neighbourhood of a solid boundary, *Journal of Fluid Mechanics* 47 (1971) 283–290.
1370

- [80] S. Zhang, J. Duncan, G. Chahine, The final stage of the collapse of a cavitation bubble near a rigid wall 257 (1993) 147–181–.
- [81] S. Zhang, J. Duncan, The behavior of a cavitation bubble near a rigid wall, in: J. R. Blake (Ed.), *Bubble Dynamics and Interface Phenomena*, 1375 Kluwer Academic Publishers, netherlands, 1994, pp. 429–436–.
- [82] A. M. Zhang, X. L. Yao, L. H. Feng, The dynamic behavior of a gas bubble near a wall 36 (2009) 295–305–.
- [83] L. Zhangrui, L. Sun, Z. Zong, Numerical analysis of gas bubbles in close proximity to a movable or deformable body 83 (2013) 1715–1737–.
- [84] G. A. Curtiss, D. M. Leppinen, Q. Wang, J. Blake, Ultrasonic cavitation 1380 near a tissue layer 730 (2013) 245–272–.
- [85] Z.-R. Li, L. Sun, Z. Zhi, J. Dong, A boundary element method for the simulation of non-spherical bubbles and the interactions near a free surface 28 (2012) 51–65–.
- [86] G. Tryggvason, R. Scardovelli, S. Zaleski, *Direct Numerical Simulations of Gas-Liquid Multiphase Flows*, Cambridge University Press, 2011. 1385
- [87] G. Chahine, Modeling of cavitation dynamics and interaction with material, in: K.-H. Kim, G. Chahine, J.-P. Franc, A. Karimi (Eds.), *Advanced Experimental and Numerical Techniques for Cavitation Erosion Prediction*, 1390 Springer, Netherlands, 2014, pp. 123–161–.
- [88] N. A. Adams, S. J. Schmidt, Shocks in Cavitating Flows, in: F. C. Delale (Ed.), *Bubble Dynamics and Shock Waves*, Springer Berlin Heidelberg, Berlin, Heidelberg, 2013, pp. 235–256.
- [89] F. Pohl, S. Mottyll, R. Skoda, S. Huth, Evaluation of cavitation-induced 1395 pressure loads applied to material surfaces by finite-element-assisted pit analysis and numerical investigation of the elasto-plastic deformation of metallic materials (article in press) (2014) –.

- [90] D. Rossinelli, B. Hejazialhosseini, P. Hadjidoukas, C. Bekas, A. Curioni, A. Bertsch, S. Futral, S. J. Schmidt, N. A. Adams, P. Koumoutsakos, 11pflop/s simulations of cloud cavitation collapse, in: SC '13 Proceedings of the International Conference on High Performance Computing, Networking, Storage and Analysis, ACM New York, Denver, CO, USA, 2013, pp. –.
- [91] B. B. Li, W. Jia, H. C. Zhang, J. Lu, Investigation on the collapse behavior of a cavitation bubble near a conical rigid boundary, *Shock Waves* 24 (2014) 317–324. doi:10.1007/s00193-013-0482-3.
- [92] B. R. Shin, Numerical simulation of cavitation bubble collapse near wall, in: A. Kuzmin (Ed.), *Computational Fluid Dynamics*, Springer-Verlag, Berlin Heidelberg, 2010, pp. –.
- [93] E. Johnsen, T. Colonius, Numerical simulations of non-spherical bubble collapse 629 (2009) 231–262–.
- [94] S. Nagrath, K. Jansen, R. Lahey, I. Akhatov, Hydrodynamic simulation of air bubble implosion using a level set approach 215 (2006) 98–132–.
- [95] E. Lauer, X. Y. Hu, S. Hickel, N. A. Adams, Numerical modelling and investigation of symmetric and asymmetric cavitation bubble dynamics, *Computers & Fluids* 69 (2012) 1–19. doi:http://dx.doi.org/10.1016/j.compfluid.2012.07.020.
- [96] N. A. Hawker, Y. Ventikos, Shock/gas bubble interactions in infinite and finite volumes of liquid (2009).
- [97] E. Maitre, Review of the numerical methods for free interfaces, Tech. rep., Laboratoire mixte de l' Ecole Polytechnique et du CNRS (2006).
- [98] S. Umemura, K. Kawabata K Fau Sasaki, K. Sasaki, In vivo acceleration of ultrasonic tissue heating by microbubble agent (2005) –.

- 1425 [99] J.-P. Franc, M. Riondet, A. Karimi, G. L. Chahine, Material and velocity effects on cavitation erosion pitting, *Wear* 274-275 (2012) 248 – 259. doi:<https://doi.org/10.1016/j.wear.2011.09.006>.
URL <http://www.sciencedirect.com/science/article/pii/S0043164811005886>
- 1430 [100] G. L. Chahine, A. Kapahi, J.-K. Choi, C.-T. Hsiao, Modeling of surface cleaning by cavitation bubble dynamics and collapse, *Ultrasonics Sonochemistry* 29 (2016) 528 – 549. doi:<https://doi.org/10.1016/j.ultsonch.2015.04.026>.
URL <http://www.sciencedirect.com/science/article/pii/S1350417715001194>
- 1435 [101] S. Hickel, M. Mihatsch, S. Schmidt, Implicit large eddy simulation of cavitation in micro channel flows, WIMRC 3rd International Cavitation Forum 2011, University of Warwick, UK, 2011.
- [102] N. Berchiche, J.-P. Franc, J.-M. Michel, A cavitation erosion model for ductile materials 124 (2002) 601–606–.
- 1440 [103] R. F. Kunz, D. A. Boger, D. R. Stinebring, T. S. Chyczewski, J. W. Lindau, H. J. Gibeling, S. Venkateswaran, T. R. Govindan, A preconditioned navier-stokes method for two-phase flows with application to cavitation prediction 29 (2000) 849–875–.
URL <GotoISI>:[//000088851200001](https://doi.org/10.1016/S00088851200001)
- 1445 [104] W. S. Senocak, I., A pressure-based method for turbulent cavitating flow computations 176(2) (2002) 363–383–.
- [105] A. Alajbegovic, H. Grogger, H. Philipp, Calculation of transient cavitation in nozzle using the two-fluid model, in: 12th ILASS-America, USA, 1999, pp. –.
- 1450 [106] G. H. Schnerr, J. Sauer, Physical and numerical modeling of unsteady cavitation dynamics (2001) –.

- [107] A. K. Singhal, M. M. Athavale, H. Y. Li, Y. Jiang, Mathematical basis and validation of the full cavitation model, in: 2001 ASME Fluid Eng. Meeting, New Orleans, USA, 2001, pp. –.
- 1455 [108] Y. Matsumoto, T. Kanbara, K. Sugiyama, Y. Tamura, Numerical study of cavitating flow structure on a hydrofoil, in: 4th KSME-JSME Fluids Eng Conf., Pusan, Korea, 1998, pp. –.
- [109] W. Yuan, G. Schnerr, Cavitation in injection nozzles - effect of injection pressure fluctuations, in: CAV2001, 4th Int. Symposium on Cavitation, 1460 Pasadena, USA, 2001, pp. –.
- [110] Y. Tamura, K. Sugiyama, Y. Matsumoto, Cavitating flow simulations based on the bubble dynamics, in: CAV2001, USA, 2001, pp. –.
- [111] A. Kubota, H. Kato, H. Yamaguchi, A new modelling of cavitating flows - a numerical study of unsteady cavitation on a hydrofoil section 240 (1992) 1465 59–96–.
- [112] E. Giannadakis, M. Gavaises, C. Arcoumanis, Modelling of cavitation in diesel injector nozzles 616 (2008) 153–193–.
- [113] A. Jamaluddin, G. Ball, C. Turangan, T. Leighton, The collapse of single bubbles and approximation of the far-field acoustic emissions for cavitation induced by shock wave lithotripsy 677 (2011) 1470 305–341–.
- [114] K. Ando, T. Colonius, C. Brennen, Numerical simulation of shock propagation in a polydisperse bubbly liquid 37 (2011) 596–608–.
- [115] D. Fuster, C. T., Modelling bubble clusters in compressible liquids 1 (2011) 1–38–.
- 1475 [116] L. Yuan, Sonochemical effects on single-bubble sonoluminescence 72 (2005) 1–14–.
- [117] W. Moss, J. Levantin, A. Szeri, A new damping mechanism in strongly collapsing bubbles 456 (2000) 2983–2994–.

- 1480 [118] J. Buitendijk, P. Pelz, The influence of imposed strain rate and circulation on bubble and cloud dynamics, in: CAV2012, Singapore, 2012.
- [119] Y. Lu, J. Katz, A. Prosperetti, Generation and transport of bubble clouds in high-intensity focused ultrasonic fields, in: CAV2012, Singapore, 2012, pp. –.
- [120] J. Dumond, F. Magagnato, A. Class, Stochastic-field cavitation model 25
1485 (2013) –.
URL <http://www.scopus.com/inward/record.url?eid=2-s2.0-84881527222&partnerID=40&md5=f9e7643457599d84a0dd1aa71eb13f2c>
- [121] M. B. Liu, J. R. Shao, Z. Shang, Sph modeling of supercavity induced
1490 by underwater high speed objects, in: 8th International Symposium on Cavitation, Singapore, 13th - 16th August, 2012, pp. –.
- [122] D. Varas, R. Zaera, J. Lopez-Puente, Numerical modelling of the hydrodynamic ram phenomenon 36 (2009) 363–374–.
URL <http://www.scopus.com/inward/record.url?eid=2-s2.0-57649187929&partnerID=40&md5=1fa1b75a20208151633b0b72e5af663f>
1495
- [123] D. M. Bourg, Development of the distributed points method with application to cavitating flow, Ph.D. thesis, PhD Thesis, University of New Orleans (2008).
- 1500 [124] G. Falcucci, S. Ubertini, G. Bella, S. Succi, Lattice boltzmann simulation of cavitating flows 13 (2013) 685–695–.
URL <http://www.scopus.com/inward/record.url?eid=2-s2.0-84866306497&partnerID=40&md5=b7acba40be3fecf3aeeb938ee1dbac39>
- 1505 [125] V. Coralic, T. Colonius, Shock-induced collapse of a bubble inside a deformable vessel 40 (2013) 64–74–.

- [126] S. Adami, J. Kaiser, I. Bernejo-Moreno, N. A. Adams, Numerical modeling of shock waves in biomedicine (nanoshock): Proceedings of the 2016 summer program, Tech. rep. (2016).
- 1510 [127] A. H. Koop, Numerical simulation of unsteady three-dimensional sheet cavitation, Ph.D. thesis, University of Twente (2008).
- [128] N. Kyriazis, P. Koukouvinis, M. Gavaises, Numerical investigation of bubble dynamics using tabulated data, *International Journal of Multiphase Flow* 93 (2017) 158 – 177. doi:<https://doi.org/10.1016/j.ijmultiphaseflow.2017.04.004>.
1515 URL <http://www.sciencedirect.com/science/article/pii/S0301932216307650>
- [129] R. A. Thompson, K.-P. Lee, R. N. Gupta, Computer codes for the evaluation of thermodynamic and transport properties for equilibrium air to
1520 30000k, Tech. rep., Langley Research Center, Hampton Virginia (1991).
- [130] B. J. McBride, G. Sanford, Computer program for calculating and fitting thermodynamic functions, Tech. rep., United States (1992).
- [131] W. C. Moss, D. B. Clarke, J. W. White, D. A. Young, Hydrodynamic simulations of bubble collapse and picosecond sonoluminescence 6 (1994)
1525 –.
- [132] M. van Rijsbergen, E.-J. Foeth, P. Fitzsimmons, A. Boorsma, High-speed video observations and acoustic-impact measurements on a naca 0015 foil, in: CAV2012, Singapore, 2012, pp. 958–964.
- [133] H. Kato, A. Konno, M. Maeda, H. Yamaguchi, Possibility of quantitative
1530 prediction of cavitation erosion without model test 118 (1996) 582–588–.
- [134] M. Mihatsch, S. Schmidt, M. Thalhamer, N. Adams, Quantitative prediction of erosion aggressiveness through numerical simulation of 3-d unsteady cavitating flows, in: 8th International Symposium on Cavitation, Singapore, 13th - 16th August, 2012, pp. –.

- 1535 [135] S. Schmidt, M. Halhamer, G. Schnerr, Inertia controlled instability and small scale structures of sheet and cloud cavitation, in: 7th International Symposium on Cavitation, Ann Arbor, MI, USA, 2009, pp. –.
- [136] Y. Wang, C. Brennen, Numerical computation of shock waves in a spherical cloud of cavitation bubbles 121 (1999) 872–880–.
- 1540 [137] S. Van Loo, T. Van Terwisga, H. Hoeijmakers, M. Hoekstra, Numerical study on collapse of a cavitating cloud of bubbles, in: CAV2012, Singapore, 2012, pp. –.
- [138] Z. Li, T. Terwisga, On the capability of multiphase rans codes to predict cavitation erosion, in: 2nd ISMP conf., Hamburg, Germany, 2011, pp. –.
- 1545 [139] Z. Li, T. Van Terwisga, On the capability of a rans method to assess the cavitation erosion risk on a hydrofoil, in: CAV2012, Singapore, 2012, pp. –.
- [140] S. R. GONZALEZ-AVILA, E. KLASEBOER, B. C. KHOO, C.-D. OHL, Cavitation bubble dynamics in a liquid gap of variable height, Journal of Fluid Mechanics 682 (2011) 241260. doi:10.1017/jfm.2011.212.
- 1550 [141] J. Choi, C.-T. Hsiao, G. Chahine, C. S, Growth, oscillation and collapse of vortex cavitation bubbles 629 (2009) 255–279–.
- [142] M. Dular, O. Coutier-Delgosha, Numerical modelling of cavitation erosion 61 (2009) 1388–1410–.
- 1555 URL <http://www.scopus.com/inward/record.url?eid=2-s2.0-74949104883&partnerID=40&md5=d0553649cfb5102b17529d0f56baec2d>
- [143] O. COUTIER-DELGOSHA, B. STUTZ, A. VABRE, S. LEGOUPIL, Analysis of cavitating flow structure by experimental and numerical investigations, Journal of Fluid Mechanics 578 (2007) 171222. doi:10.1017/S0022112007004934.
- 1560

- [144] F. J. Heymann, High speed impact between a liquid drop and a solid surface, *Journal of Applied Physics* 40 (13) (1969) 5113–5122. arXiv:
<http://dx.doi.org/10.1063/1.1657361>, doi:10.1063/1.1657361.
1565 URL <http://dx.doi.org/10.1063/1.1657361>
- [145] M. B. Lesser, Analytic solutions of liquid-drop impact problems, *Proceedings of the Royal Society of London A: Mathematical, Physical and Engineering Sciences* 377 (1770) (1981) 289–308. doi:10.1098/rspa.1981.0125.
- 1570 [146] K. K. Haller, Y. Ventikos, D. Poulikakos, P. Monkewitz, Computational study of high-speed liquid droplet impact, *Journal of Applied Physics* 92 (5) (2002) 2821–2828. arXiv:<http://dx.doi.org/10.1063/1.1495533>, doi:10.1063/1.1495533.
URL <http://dx.doi.org/10.1063/1.1495533>
- 1575 [147] A. V. Chizhov, K. Takayama, The impact of compressible liquid droplet on hot rigid surface, *International Journal of Heat and Mass Transfer* 47 (67) (2004) 1391 – 1401. doi:<https://doi.org/10.1016/j.ijheatmasstransfer.2003.05.001>.
URL <http://www.sciencedirect.com/science/article/pii/S0017931003005659>
1580
- [148] T. Sanada, K. Ando, T. Colonius, A computational study of high-speed droplet impact, *Fluid Dynamics and Materials Processing* 7 (4) (2011) 329–340. doi:10.3970/fdmp.2011.007.329.
- [149] Y.-Y. Niu, H.-W. Wang, Simulations of the shock waves and cavitation
1585 bubbles during a three-dimensional high-speed droplet impingement based on a two-fluid model, *Computers & Fluids* 134135 (2016) 196 – 214. doi:<http://doi.org/10.1016/j.compfluid.2016.05.018>.
URL <http://www.sciencedirect.com/science/article/pii/S0045793016301657>

- 1590 [150] G. Lacaze, A. Misdariis, A. Ruiz, J. C. Oefelein, Analysis of high-pressure
diesel fuel injection processes using les with real-fluid thermodynamics
and transport, *Proceedings of the Combustion Institute* 35 (2) (2015)
1603–1611.
URL [http://www.sciencedirect.com/science/article/pii/
1595 S1540748914002302](http://www.sciencedirect.com/science/article/pii/S1540748914002302)
- [151] F. Örley, T. Trummler, S. Hickel, M. S. Mihatsch, S. J. Schmidt, N. A.
Adams, Large-eddy simulation of cavitating nozzle flow and primary
jet break-up, *Physics of Fluids* 27 (8) (2015) 086101. [arXiv:http:
//aip.scitation.org/doi/pdf/10.1063/1.4928701](http://arxiv.org/abs/1508.08610), doi:10.1063/1.
1600 4928701.
URL <http://aip.scitation.org/doi/abs/10.1063/1.4928701>
- [152] A. Gnanaskandan, K. Mahesh, A numerical method to simulate turbulent
cavitating flows, *International Journal of Multiphase Flow* 70 (2015) 22
– 34. doi:[https://doi.org/10.1016/j.ijmultiphaseflow.2014.11.
1605 009](https://doi.org/10.1016/j.ijmultiphaseflow.2014.11.009).
URL [http://www.sciencedirect.com/science/article/pii/
S0301932214002298](http://www.sciencedirect.com/science/article/pii/S0301932214002298)
- [153] C. Greenshields, *OpenFOAM - The Open Source CFD Toolbox - User
Guide*, OpenFOAM Foundation Ltd., 2nd Edition (21 May 2015).
- 1610 [154] G. H. Schnerr, I. H. Sezal, S. J. Schmidt, Numerical investigation of three-
dimensional cloud cavitation with special emphasis on collapse induced
shock dynamics, *Physics of Fluids* 20 (4) (2008) 040703. [arXiv:https:
//doi.org/10.1063/1.2911039](http://arxiv.org/abs/0804.0703), doi:10.1063/1.2911039.
URL <https://doi.org/10.1063/1.2911039>
- 1615 [155] P. Koukouvinis, H. Naseri, M. Gavaises, Performance of turbulence
and cavitation models in prediction of incipient and developed cavi-
tation, *International Journal of Engine Research* 18 (4) (2017) 333–
350. [arXiv:https://doi.org/10.1177/1468087416658604](http://arxiv.org/abs/1704.08604), doi:10.

1177/1468087416658604.

1620 URL <https://doi.org/10.1177/1468087416658604>

- [156] J.-P. Franc, J.-M. Michel, Fundamentals of Cavitation, Kluwer Academic Publishers, 2005.
- [157] V. der Heul, D. R., C. Vuik, P. Wesseling, Efficient computation of flow with cavitation by compressible pressure correction, Barcelona, 2000.
- 1625 [158] C. D. Munz, S. Roller, R. Klein, K. J. Geratz, The extension of incompressible flow solvers to the weakly compressible regime, Computers & Fluids 32 (2003) 173–196.
- [159] H. Guillard, C. Viozat, On the behaviour of upwind schemes in the low mach number limit, Computers & Fluids 28 (1999) 63–86.
- 1630 [160] A. Meister, Asymptotic single and multiple scale expansions in the low mach number limit, SIAM Journal on Applied Mathematics 60 (1999) 256–271.
- [161] E. F. Toro, Riemann Solvers and Numerical Methods for Fluid Dynamics, A Practical Introduction, Springer Berlin Heidelberg, 2009.
- 1635 [162] S. Schmidt, I. Sezal, G. Schnerr, M. Talhamer, Riemann techniques for the simulation of compressible liquid flows with phase-transition at all mach numbers - shock and wave dynamics in cavitating 3-d micro and macro systems, Aerospace Sciences Meetings, American Institute of Aeronautics and Astronautics, 2008. doi:10.2514/6.2008-1238.
- 1640 URL <http://dx.doi.org/10.2514/6.2008-1238>
- [163] F. Moukalled, L. Mangani, M. Darwish, The Finite Volume Method in Computational Fluid Dynamics, An Advanced Introduction with OpenFOAM and Matlab, Vol. 113, Springer International Publishing, 2015. doi:10.1007/978-3-319-16874-6.

- 1645 [164] R. Abgrall, R. Saurel, Discrete equations for physical and numerical compressible multiphase mixtures, *Journal of Computational Physics* 186 (2) (2003) 361 – 396. doi:[https://doi.org/10.1016/S0021-9991\(03\)00011-1](https://doi.org/10.1016/S0021-9991(03)00011-1).
URL <http://www.sciencedirect.com/science/article/pii/S0021999103000111>
- 1650 [165] R. Saurel, F. Petitpas, R. Abgrall, Modelling phase transition in metastable liquids: application to cavitating and flashing flows, *Journal of Fluid Mechanics* 607 (2008) 313–350.
URL <https://www.cambridge.org/core/article/modelling-phase-transition-in-metastable-liquids-application-to-cavitating-and-flashing>
1655 [00A5620371349920CEAD54065D60011E](https://www.cambridge.org/core/article/modelling-phase-transition-in-metastable-liquids-application-to-cavitating-and-flashing)
- [166] P. Koukouvinis, M. Gavaises, A. Georgoulas, M. Marengo, Compressible simulations of bubble dynamics with central-upwind schemes, *International Journal of Computational Fluid Dynamics* (2016) 1–12.
- 1660 [167] W. Wagner, A. Pru, The iapws formulation 1995 for the thermodynamic properties of ordinary water substance for general and scientific use, *Journal of Physical and Chemical Reference Data* 31 (2) (2002) 387–535. arXiv:<http://dx.doi.org/10.1063/1.1461829>, doi:10.1063/1.1461829.
1665 URL <http://dx.doi.org/10.1063/1.1461829>
- [168] E. Lemmon, M. McLinden, D. Friend, NIST Chemistry WebBook, NIST Standard Reference Database Number 69, 2005, Ch. Thermophysical properties of fluid systems.
URL <http://webbook.nist.gov>

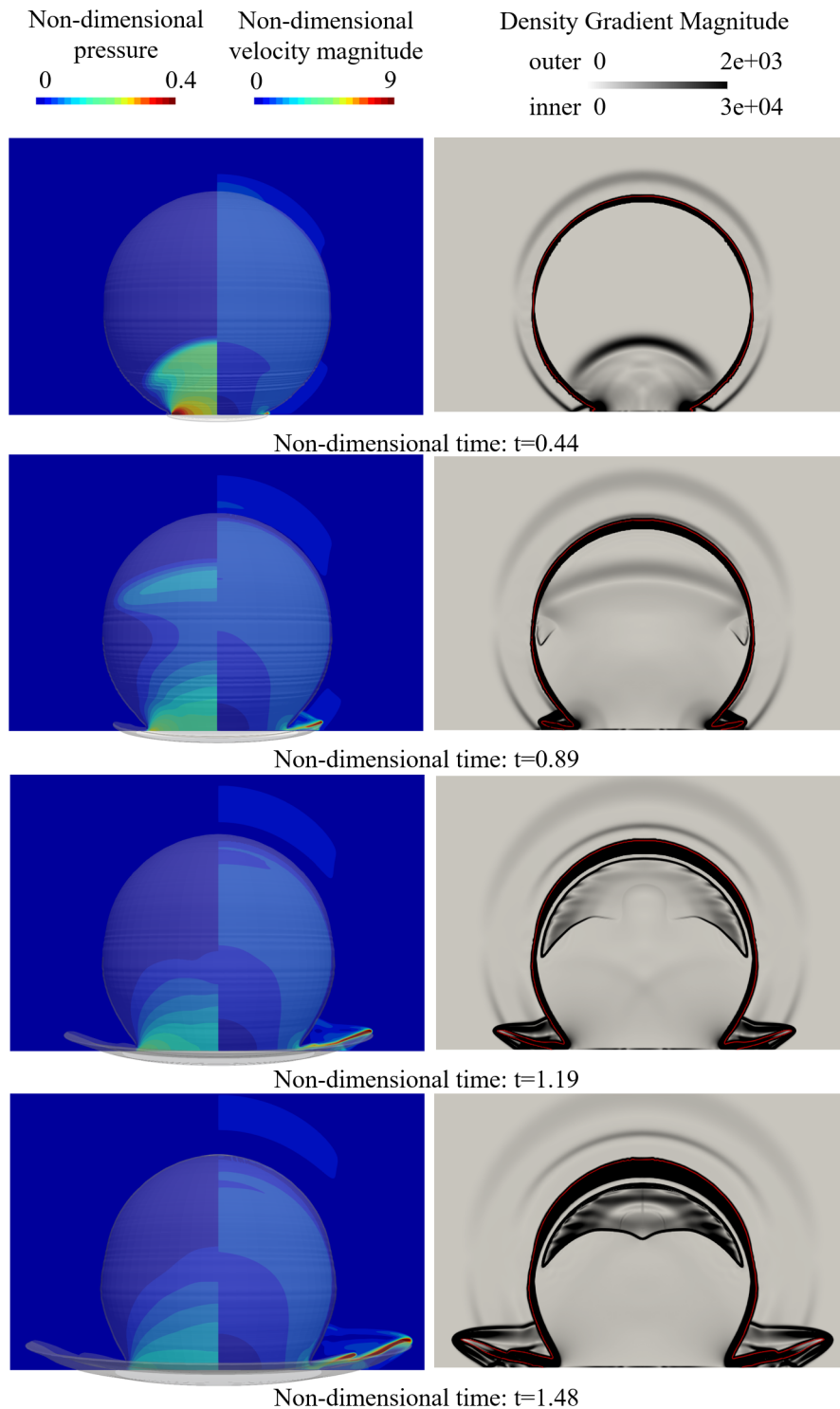


Figure 5: Drop impact at velocity 110 m/s . Left figure: Iso-surface of liquid mass fraction for $Y_g = 0.5$ combined with pressure (left slice) and velocity magnitude (right slice). Right figure: Density gradient magnitude, different scale for the interior and the exterior of the droplet. Pressure and velocity are divided by p_{wh} and u_{imp} respectively, whereas time is measured from the moment of the impact and it has been non-dimensionalized with D/c_l .

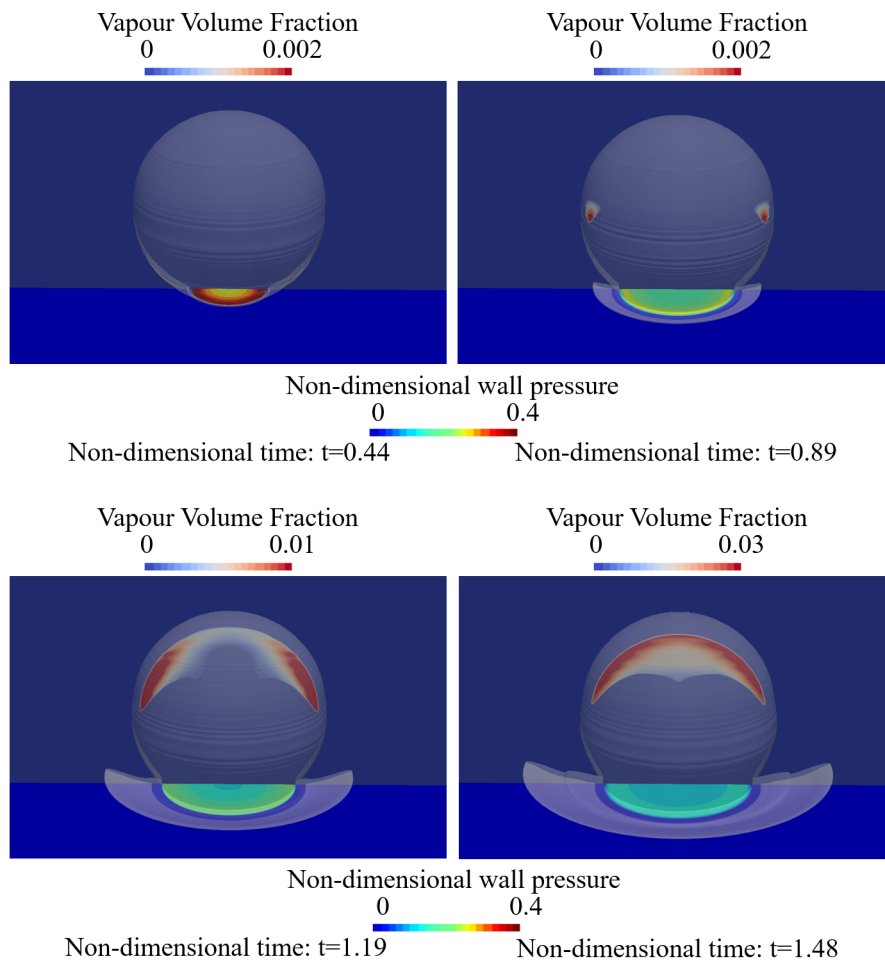


Figure 6: Drop impact at velocity 110 m/s . Iso-surface of liquid mass fraction for $Y_g = 0.5$ combined with wall pressure (bottom slice) and vapour volume fraction (upper slice). Pressure is divided by p_{wh} and time is measured from the moment of the impact and it has been non-dimensionalized with D/c_l .

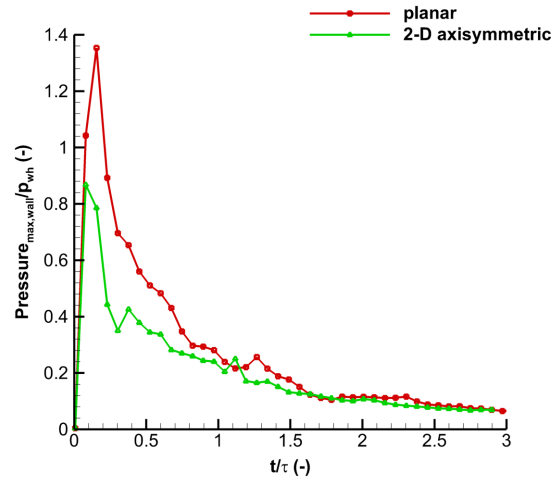


Figure 7: Comparison of the maximum wall pressure between a planar 2-D and a 2-D axisymmetric simulation at impact velocity 110 m/s . Wall pressure is non-dimensionalized with p_{wh} and time is measured from the moment of the impact and it has been non-dimensionalized with $\tau = D/c_l$.

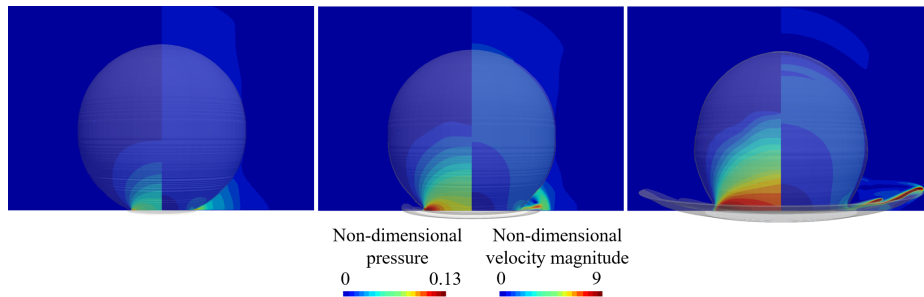


Figure 8: Comparison of the pressure (left slice) and the velocity magnitude (right slice) for $u_{imp} = 22.5\text{ m/s}$ (left), $u_{imp} = 55\text{ m/s}$ (middle) and $u_{imp} = 110\text{ m/s}$ (right) at non dimensional time $t = 1.48$. The iso-surface of liquid mass fraction for $Y_g = 0.5$ is also shown. Pressure and velocity are divided by p_{wh} and u_{imp} respectively, whereas time is measured from the moment of the impact and it has been non-dimensionalized with D/c_l .

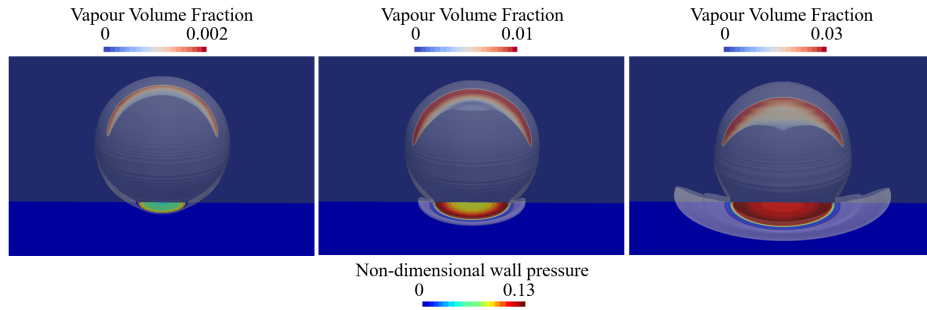


Figure 9: Comparison of the vapour volume fraction (upper) and wall pressure (bottom) for $u_{imp} = 22.5 \text{ m/s}$ (left), $u_{imp} = 55 \text{ m/s}$ (middle) and $u_{imp} = 110 \text{ m/s}$ (right) at non dimensional time $t = 1.48$. The iso-surface of liquid mass fraction for $Y_g = 0.5$ is also shown. Pressure is divided by p_{wh} and time is measured from the moment of the impact and it has been non-dimensionalized with D/c_l .

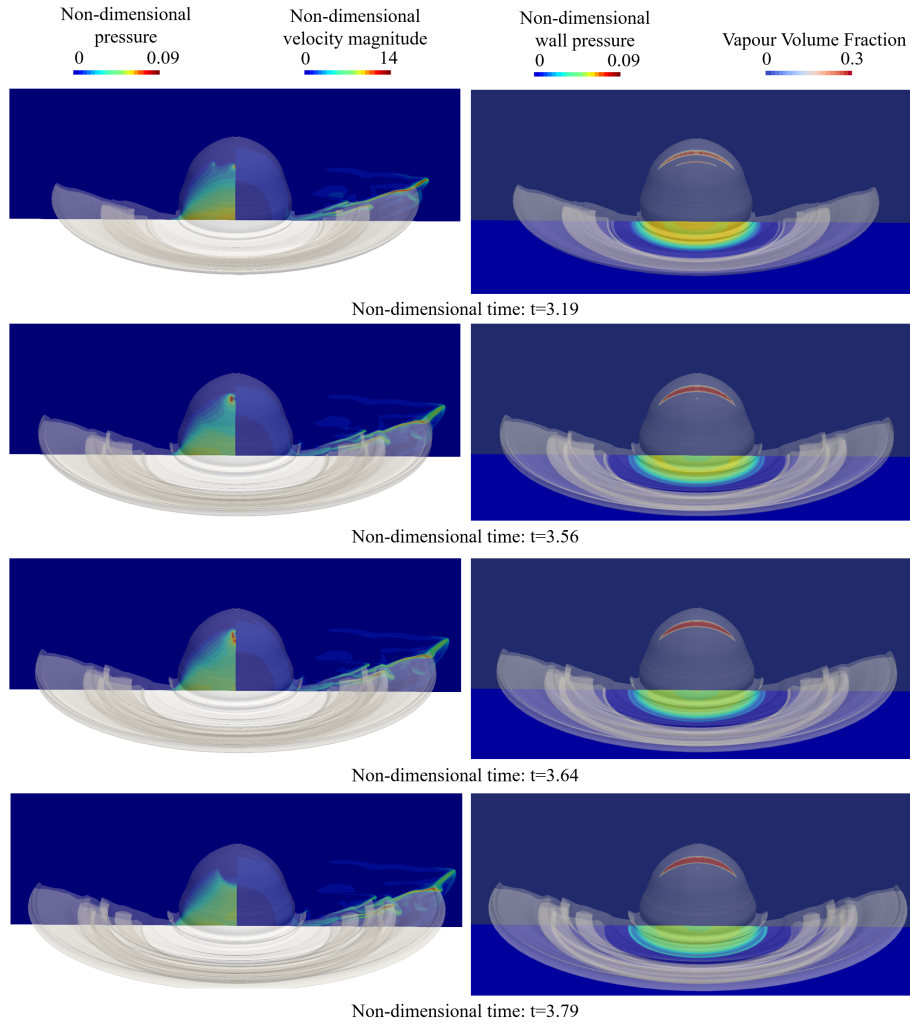


Figure 10: Later stage of droplet impact at velocity 110 m/s . Left figure: Iso-surface of liquid mass fraction for $Y_g = 0.5$ combined with pressure (left slice) and velocity magnitude (right slice). Right figure: Iso-surface of liquid mass fraction for $Y_g = 0.5$ combined with wall pressure (bottom slice) and vapour volume fraction (upper slice). Pressure and velocity are divided by p_{wh} and u_{imp} respectively, whereas time is measured from the moment of the impact and it has been non-dimensionalized with D/c_l .

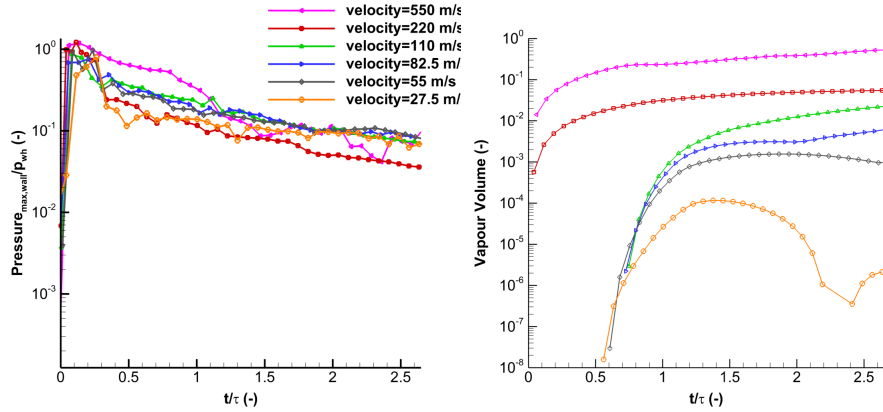


Figure 11: Maximum wall pressure (left) and generated vapour volume (right) with respect to time for different impact velocities. Wall pressure is divided by p_{wh} , time is measured from the moment of the impact and it has been non-dimensionalized with $\tau = D/c_l$, whereas vapour volume is divided by the initial droplet volume.

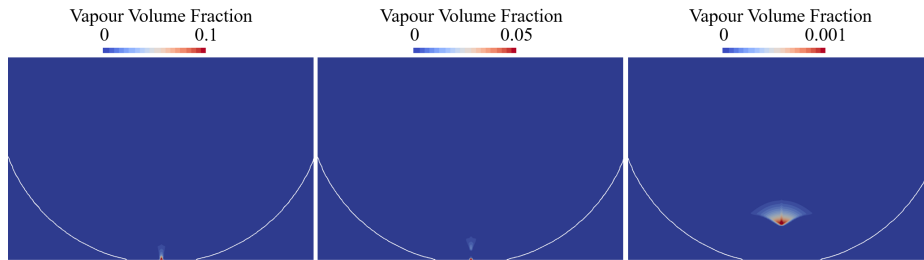


Figure 12: Close-up view of *case 8* at non-dimensional times $t = 0.15$ (left), $t = 0.18$ (medium) and $t = 0.25$ (right). Slices of vapour volume fraction combined with iso-line of liquid mass fraction for $Y_g = 0.5$ are shown. Time has been non-dimensionalized with D/c_l .

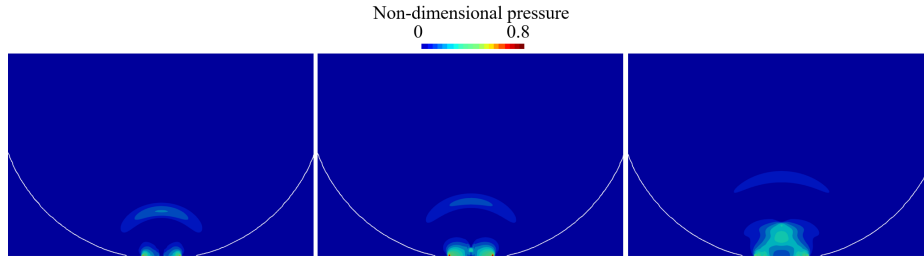


Figure 13: Close-up view of *case 8* at non-dimensional times $t = 0.15$ (left), $t = 0.18$ (medium) and $t = 0.25$ (right). Slices of pressure combined with iso-line of liquid mass fraction for $Y_g = 0.5$ are shown. Time has been non-dimensionalized with D/c_l and pressure with p_{wh} .

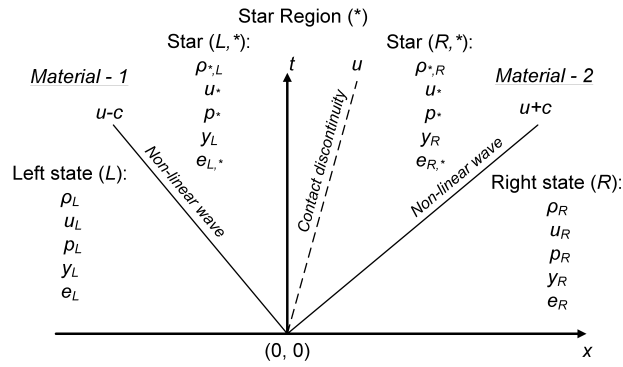


Figure A.14: Wave structure of the Riemann problem for the multi-material Euler equations for a general equation of state $p = f(\rho, e, Y)$.

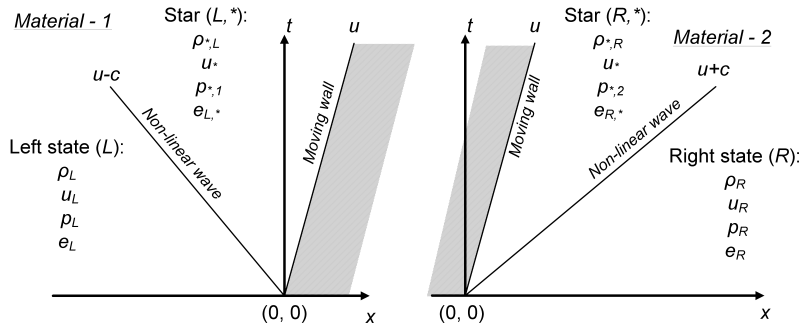


Figure A.15: Equivalent splitting of the multi-material Riemann problem to two coupled single-material Riemann problems.